University of Twente

EEMCS / Electrical Engineering
Control Engineering

Design and control of a modular end-effector for UAVs in interaction with a remote environment

J.T. (Teun) Bartelds

BSc Report

Committee:
Prof. dr. ir. S. Stramigioli
Dr. R. Carloni
Dr. M. Fumagalli
Prof. dr. ir. A. de Boer

July 2012

Report nr. 015CE2012
Control Engineering
EE-Math-CS
University of Twente
P.O. Box 217
7500 AE Enschede
The Netherlands

List of contents

Abstract

Service tasks on large infrastructural or industrial structures, e.g. inspection of bridges on structural integrity or window cleaning of skyscrapers, usually entail laborious and expensive support structures and hazardous working environments. Recent developments on UAVs interacting with their environment offer many new possibilities, leading to service robotics becoming airborne.

Within the AIRobots project [1], a European collaboration in the field of innovative aerial service robots, a manipulation system was developed to endow a UAV for interactive tasks. For this manipulator a delta structure with 3 degrees of freedom was chosen, because of the advantages of the parallel kinematics compared to serial equivalents. In sequel to this project a versatile end-effector must be developed to make full use of the broad range of possible applications the system can offer.

This work covers the design of a modular end-effector capable of executing a large variety of service and maintenance tasks. Two task specific modules are elaborated: a non-destructive testing (NDT) sensor and a versatile underactuated gripper. The permanently attached basis of this modular system, i.e. the end-effector, has 3 degrees of freedom to improve the interaction stability of UAVs with unknown environments. This system is suspended with a pre-tensionable passive spring system in order to provide a stable and adaptable zero reference position, which is modelled, designed and realized. The NDT module, having one additional, actuated degree of freedom, has also been designed and realized in a lightweight prototype. The underactuated gripping module has not yet been realized apart from a preliminary 3D printed version, though a novel design is proposed, employing a variable stiffness actuator in order to gain control over the contact force distribution.

I. Introduction

For service tasks on large infrastructural or industrial structures great efforts are usually needed. In general laborious and expensive support structures, e.g. scaffoldings, are necessary to reach otherwise inaccessible locations. Consider for instance the inspection of bridges on structural integrity, maintenance activities on industrial boilers or chimneys, applying sprayable coatings to protect metal structures from corroding or cleaning skyscraper windows. Such environments remain very hazardous to humans, even under the most thorough safety regulations.

These challenges lead to the development of innovative robotic vehicles being either fully autonomous or (partially) remote controlled. Wheeled, tracked or legged robots remain limited to the ground and would need to be equipped with additional climbing functionality to encounter large structures. Research has shown successful attempts on wall climbing robots using magnetic [2] [3] or aerostatic forces [4] [5] to clamp themselves to the structure, but these solutions are limited to specific structures and surface irregularities remain problematic in many occasions.

Unmanned Aerial Vehicles (UAVs) have proven to be much more successful in reaching otherwise inaccessible places and in executing priorly described service, measurement, or exploration tasks. UAVs do not need to interact with the structure in order to reach a specific location, making them very widely applicable in contrary to climbing robots. It is clear that their mobility is a great advantage, but for most tasks to be performed interaction with the structure, which is not trivial for an underactuated flying vehicle, is unavoidable. Resent research on UAVs interacting with their environment, e.g. (figure 1) a quadrotor in stable contact with a wall through a rigid extension [6] and one equipped with a manipulation system [7], already reveal some of the numerous possibilities in this relatively new field of research. Especially the latter, employing a fully actuated 3 DOF delta structure seems very promising for the near future, because of its high position accuracy compared to rigid extensions.

To make full use of the broad range of applications a manipulator endowed UAV can offer, the end-effector of the manipulation system designed within the AIRobots project was redesigned into a modular, i.e. easily interchangeable, system. This system consist of a permanently attached end-effector (section II), and several task specific modules, of which two are elaborated: a support for a non-destructive testing sensor (section III) and an underactuated gripper (section IV). In the end the conclusions and future work is discussed (section V). This continuation has been executed, just like the previous work, within the AIRobots project [1].

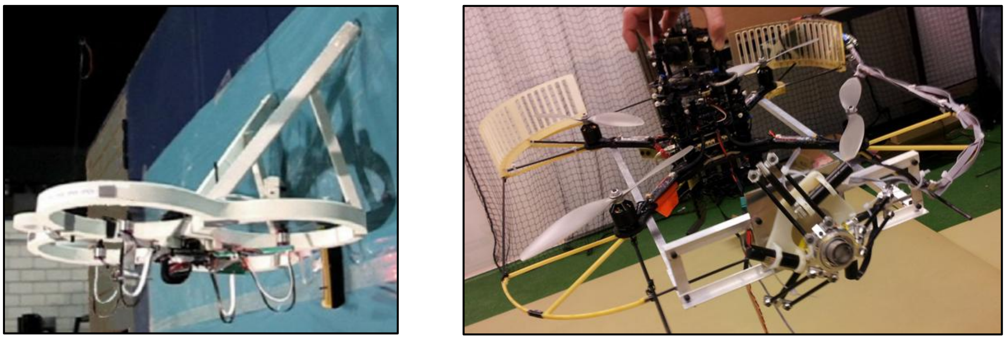

Figure 1: Quadrotor UAVs endowed with a rigid extension (left) and an actuated manipulation system (right) to interact with its environment. *Sources:* **[6] [7]**

II. End-effector

In this section the requirements, modelling, design and realization of the new, modular end-effector are elaborated. In total three end-effectors are referred to, named in chronological order EE1, EE2 and EE3, corresponding to respectively the last end-effector designed within the AIRobots project (figure 2) [8], the conceptual redesign of this prototype and the final version of the redesign.

a. Previous work

This subsection summarizes the previous work done on the manipulation system within the AIRobots project [1] [7] [8]. Figure 2 depicts the prototype of the delta structured manipulator and its end-effector carrying an Ultrasonic Testing (UT) sensor.

Figure 2: A picture of the previous designed manipulation system including the end-effector (EE1).

The delta structure provides 3 DOFs in Cartesian space, fully actuated by 3 DC motors placed at the baseplate. The shins form a parallelogram that constrains the outer ring of the end-effector, thereby making sure it always remains parallel to the baseplate of the manipulator. The thighs have a milled out aluminium component near the motor attachment, where strain gages are applied to measure the motor torques, which can be used for the system's control.

Figure 3 shows an exploded view of the end-effector, denoting all important parts. The UT sensor, denoted with number 1, is used for Non Destructive Testing (NDT) tasks. Parts 2 – 4 form a 2 DOF passive gimbal joint, allowing the end-effector to properly align with a wall despite misalignment or hovering motions of the UAV. To provide a stable zero reference angle, three elastic bands connect the bottom of the inner gimbal part to the outer gimbal ring. The next part, denoted with number 5, gives the end-effector a passive translational DOF, to decouple the sensor from the rest of the UAV during impact. At last number 6 indicates the actuation mechanism for the last DOF, i.e. the actuated roll rotation of the sensor, needed for proper measurements.

A prototype was realized from which the following conclusions were drawn. The gimbal system proved to work properly, but the elastic bands failed in their contribution to a stable reference position. The lack of adjustability leads to an inaccurate equilibrium position and also the bands snapped multiple times during tests. Furthermore parts 4 – 6 might be combined to make the system much more compact.

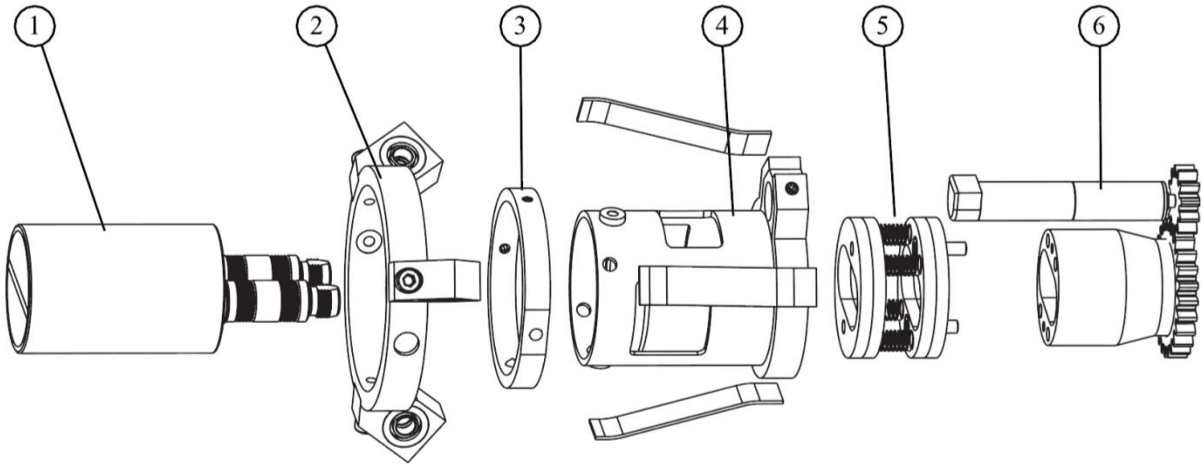

Figure 3: An exploded view of EE1; 1. NDT-UT sensor, 2. outer gimbal ring to which the legs of the manipulator are connected, 3. middle gimbal ring, 4. Inner gimbal part with the motor attachment and three elastic bands, 5. spring section containing four compression springs, 6. the mini DC motor and bottom part that holds the sensor.

b. Requirements

Interaction – The system should contain 2 rotational degrees of freedom in order to keep the carried module parallel to the inspected wall despite hovering movements or misalignments of the UAV. Furthermore 1 translational degree of freedom is needed to decouple the end-effector module from the rest of the UAV providing softer impacts and better system dynamics when interacting.

Lightweight – The total weight of the manipulator, end-effector and possibly carried objects should not exceed the maximum payload of the UAV. The end-effector's weight should thus be minimized. The resulting system should weigh less or the same as the previously designed end-effector prototype (EE1), i.e. $m_{ee,3} \leq m_{ee,1} \approx 34\ grams$.

Compact – The end-effector should not confine the manipulator's workspace of $5 \times 5 \times 5\ cm^3$, hence a compact design is needed. Furthermore, all carried modules should fit inside the end-effector, including the Non Destructive Testing sensor used with EE1. Hence the inner diameter of the end-effector should remain $20\ mm$.

Compatible – Obviously the redesigned end-effector should be compatible with the rest of the manipulation system of EE1. This means that the legs of the delta structure should be attached to the end-effector's outer ring at exactly the same positions, since otherwise the delta structure's kinematics is influenced.

Versatile – The end-effector should be extremely versatile, i.e. capable of executing a large variety of tasks. This will be achieved by a smart end-effector design in which various end-effector modules can be placed. In order for this system to be advantageous, quick and easy replacement of the different modules is a necessity.

Robust – The system must be robust in order to survive in-flight collisions while hovering near a structure. Besides the intended contact forces up to approximately $5\ N$, impact forces up to $20N$ should be handled without causing damage to the end-effector itself, nor to the carried task specific module, nor to the mechanical connection between both parts.

c. Conceptual design

The basic concept of the end-effector (figure 3) remains the same, a double gimbal joint providing the two rotational DOFs, however some improvements are carried out in order to make the system more robust, more compact and modular. Due to the modular design the NDT-UT sensor is omitted in the rest of this section, but will return as a separate module in section III.

The elastic bands, as well as the 4 compression springs are replaced by 3 tension springs, resulting in a more robust and more compact design. In order to unite the functions of both spring systems, one part is needed with both the 2 translational DOFs as well as the translational DOF. Figure 4 depicts an exploded view in which number 5 denotes this slider part with the spring attachments. The other ends of the springs will be attached to the part denoted with number 1, a pre-tensioning system allowing to provide a stable zero reference for different end-effector modules with different mass distributions.

The gimbal rings can be turned and milled from aluminium, considering the good results of the previous prototype, but since aluminium on aluminium results in high friction and wear another material must be considered for the slider part. This can be for instance another metal, e.g. brass, which is very heavy, or a (self-lubricating) plastic, which is a much lighter solution, but might be harder to process.

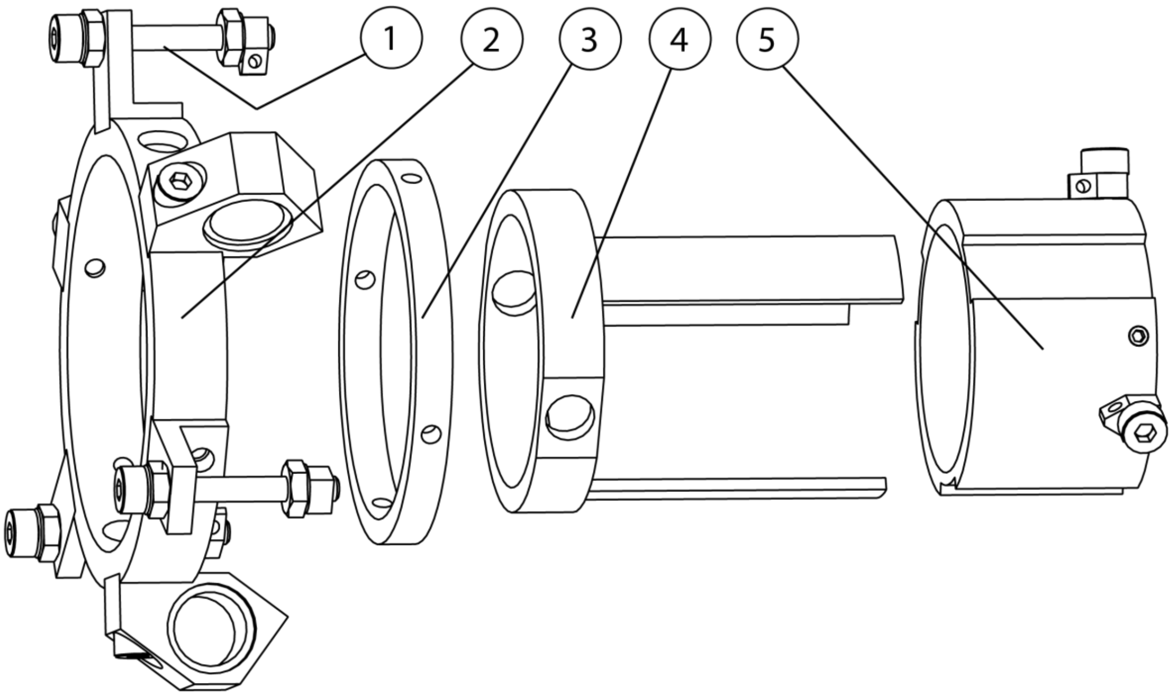

Figure 4: An exploded view of EE2; 1. pre-tensioning system to which one end of the spring is attached, 2. outer gimbal ring, 3. middle gimbal ring, 4. inner gimbal ring with three legs to guide the slider, 5. slider part with slots to prevent rotation with respect to the inner gimbal and with attachments for the other end of the springs.

d. Modelling

A two dimensional representation was modelled to predict the behaviour of this conceptual design and investigate the influence of the pre-tensioning angle (α). In this representation only two DOFs remain: a translation along the slider's longitudinal axis, denoted with x, and a rotation around an axis perpendicular to the model, denoted with θ. Both DOFs are mechanically bounded to $[0,10]\ mm$ and $[-30,30]°$ respectively.

By means of a static model, which is sufficient to reach its goal, we can find expressions for F_x and M_{cr}, which are the efforts , i.e. force and moment, in x and θ direction:

$$\begin{cases} F_x \ = (k_1 + k_2)x + (k_2 - k_1)r_g\, sin(\theta) + (p_1 + p_2)\, cos(\theta + \alpha) \\ M_{cr} = (k_1 + k_2) \cdot r_s r_g\, sin(\theta) + (k_2 - k_1) \cdot \left[r_s x + r_g(l_s + x) \cdot (cos(\theta) - 1)\right] + \\ \qquad +(p_2 - p_1) \cdot [r_s\, cos(\theta + \alpha) + (l_s + x)\, sin(\theta + \alpha)] \end{cases}$$

In which k_i is the spring constant and p_i the pre-tensioning load of spring i. Furthermore, the slider radius (r_s), gimbal radius (r_g) and slider length (l_s) can be found in this expression.

When looking at the zero reference configuration, i.e. $\theta = 0$ and $x = 0$, these equations simplify to:

$$\begin{cases} F_x(\theta = 0, x = 0) = (p_1 + p_2)\, cos(\alpha) \\ M_{cr}(\theta = 0, x = 0) = (p_2 - p_1) \cdot [r_s\, cos(\alpha) + l_s\, sin(\alpha)] \end{cases}$$

These equations appear to be very useful, since the pre-tensioning is employed to provide a stable zero reference position, hence it is important to know the influence of α in this position.

Concerning the perceived stiffness of the system in direction of the corresponding DOF for a given position the following equations can be derived:

$$\begin{cases} k_x = k_1 + k_2 \\ k_\theta = (k_1 + k_2) \cdot r_s r_g \cos(\theta) - (k_2 - k_1) \cdot r_g(ls + x) \cdot \sin(\theta) + \\ \qquad +(p_2 - p_1) \cdot [(l_s + x) \cdot cos(\theta + \alpha) - r_s \cdot sin(\theta + \alpha)] \end{cases}$$

Where k_x turns out to be constant, no matter which configuration or pre-tensioning angles or loads are chosen. k_θ obviously shows more complicated behaviour, which will be further examined in the next subsection.

Since this short section does not cover all the details, a full description of the model, its derivation and implementation in Matlab have been added in appendix A.

e. Results

The results from a simulation with the priorly described model is discussed in this subsection. All design parameters were chosen in line with the conceptual design described in subsection c, however the pre-tensioning angle and value will remain variable:

$$r_g = 23.55\,mm \qquad r_s = 13.09\,mm,$$
$$l_s = 13\,mm \qquad k_1 = k_2 = 0.2\,N/mm$$
$$\alpha \in [0{,}90]^\circ \qquad x_{pt,1} \in [0{,}10]\,mm$$

$x_{pt,2}$ is kept zero, since pre-tensioning is only useful to generate a moment in asymmetric situations. Instead the roles of spring 1 and 2 could be switched, delivering the same results, mirroring the graphs of figure 6 in the line $\theta = 0$, i.e. changing the sign of θ.

Since there are still 4 variables, many different graphs can be made, however only the most interesting are discussed here. The figures shown on the right are built up similarly: every plot contains six coloured lines corresponding to $x_{pt,1} = \{0{,}2{,}4{,}6{,}8{,}10\}$, of which the zero pre-tension is the same for all values of α and is coloured green.

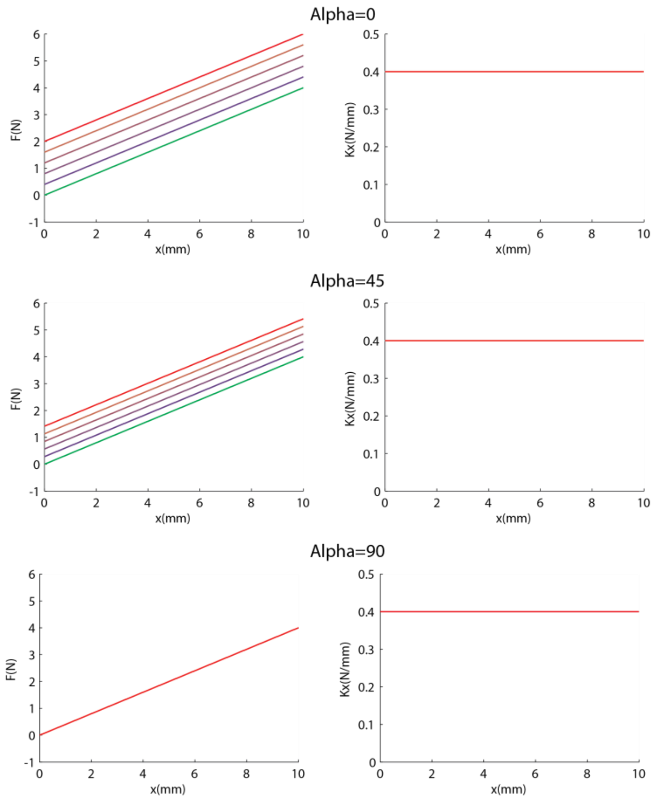

Figure 5: Plots of $\boldsymbol{F_x(x)}$ and $\boldsymbol{k_x(x)}$ for $\boldsymbol{x_{pt,1} = 0\,mm}$ (green) to $\boldsymbol{10\,mm}$ (red), $\boldsymbol{\theta = 0^\circ}$ and $\boldsymbol{\alpha = \{0, 45, 90\}^\circ}$

Figure 5 shows the plots of F_x and k_x as a function of x. The pre-tensioning angle does not influence the behaviour of the system. The stiffness is constant, as expected, and exactly equal to the sum of the spring constants. The configuration with $\alpha = 90^\circ$ is ideal, since pre-tensioning does not influence F_x at all, however the influence at other angles is not very large, so these configurations are also possible.

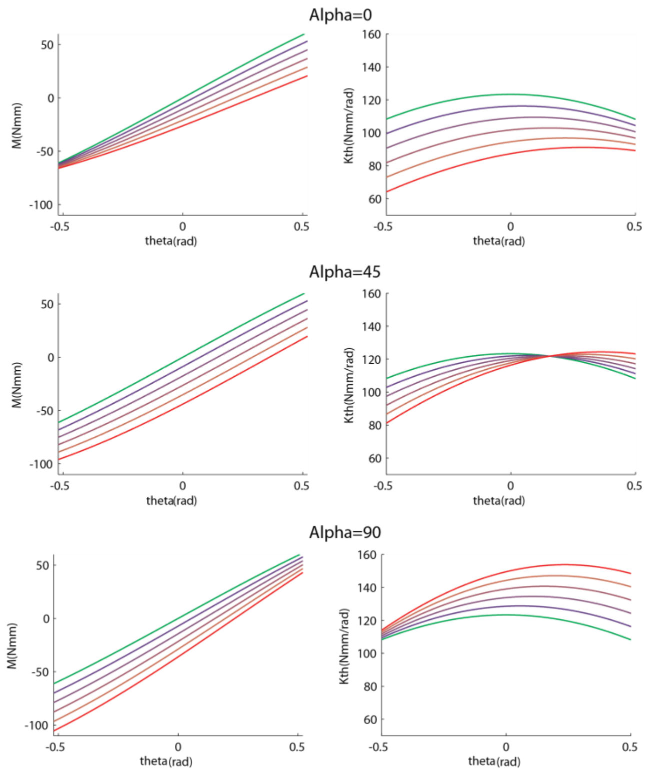

Figure 6: Plots of $\boldsymbol{M(\theta)}$ and $\boldsymbol{k_\theta(\theta)}$ for $\boldsymbol{x_{pt,1} = 0\,mm}$ (green) to $\boldsymbol{10\,mm}$ (red), $\boldsymbol{x = 5}$ and $\boldsymbol{\alpha = \{0, 45, 90\}^\circ}$

Figure 6 shows the same plots for M_{cr} and k_θ as a function of θ. First of all it can be noticed that pre-tensioning has the desired effect, since the zero crossing, i.e. static equilibrium, shifts due to the increasing pre-tension. Or, when looking at $\theta = 0$ a larger negative moment can be generated.

Furthermore it can be seen from the plots for $\alpha = 0°$ and for $\alpha = 45°$, that the perceived stiffness decreases for increasing pre-tension. If the pre-tension would be increased further, the stiffness would become negative eventually, leading to an instable situation. However, for these configurations and this pre-tension range this is not the case, so still all values for α are allowed.

When looking a figure 7, a plot of the moment that can be generated in zero reference position, i.e. $M_{cr}(0,0) = (p_2 - p_1)[r_s \cos(\alpha) + l_s \sin(\alpha)]$, we see that for $\alpha \approx 45°$ the generated moment is maximal. However, for α is 0 and 90 degrees the generated moments are still $2 \cdot r_s = 26.2\ Nmm$ and $2 \cdot l_s = 26.0\ Nmm$ respectively, which is easily sufficient to balance the moment due to gravity on the slider ($\approx 5.5\ Nmm$ for the NDT-sensor).

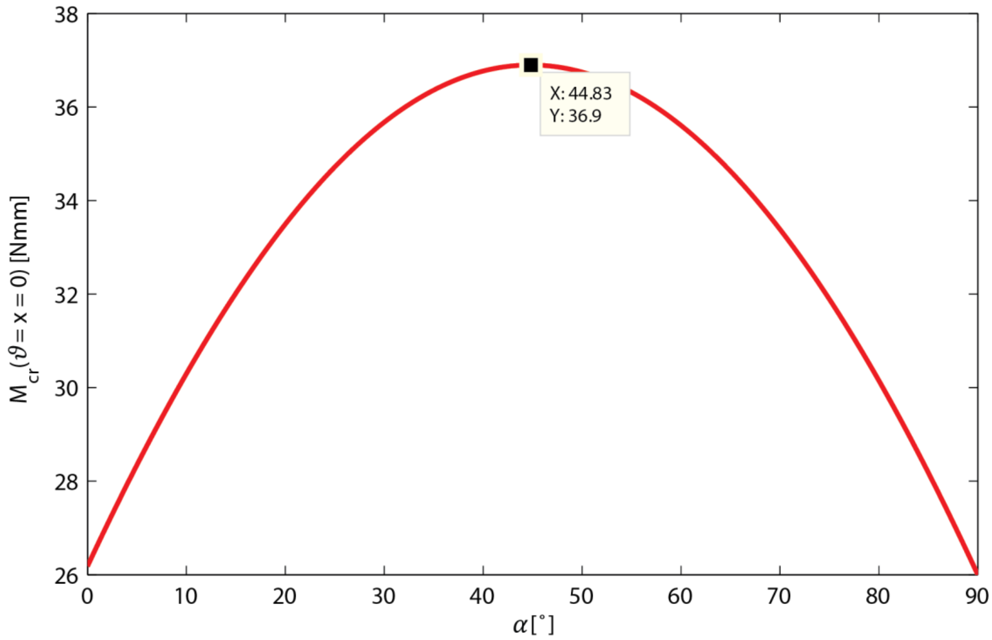

Figure 7: a plot of the generated moment in zero reference position generated under maximal pre-tension

It can be concluded that all values of $\alpha \in [0,90]°$ result in a properly functioning system, where values of 45 and 90° have (minor) benefits. However, from a design point of view $\alpha = 0°$ is favourable, since it results in the most compact design. Since compactness is more advantageous than a slightly larger moment or less influence on the translational DOF, the pre-tensioning system can be maintained at an angle of zero degrees.

f. Final design and realization

In the previous section a proof of concept is given for the conceptual design, hence the basic functioning can be maintained and some small changes are made to improve the producibility. The technical drawings of all parts of this final design can be found in appendix B.

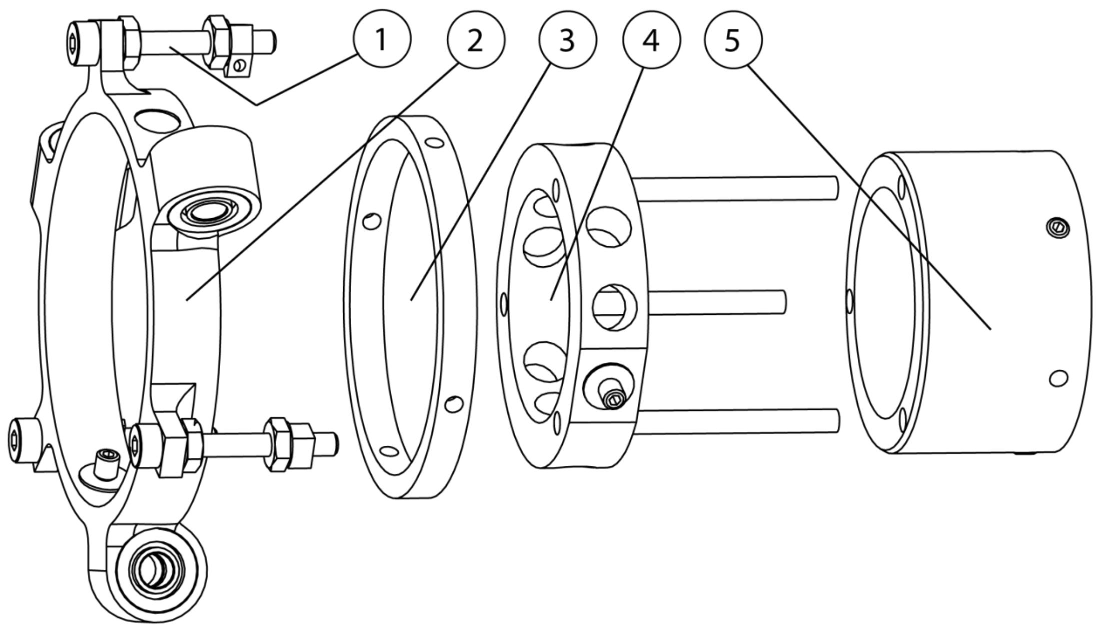

Figure 8: An exploded view of EE3; 1. pre-tensioning system to which one end of the spring is attached, 2. outer gimbal ring, 3. middle gimbal ring, 4. inner gimbal ring with three rods to guide the slider, 5. slider part with holes all along the length and with six radial distributed, threaded holes to attach the springs and clamp the end-effector module.

Two major changes have been carried through. The inner gimbal now holds three steel rods as guides for the slider. Due to this the gimbal ring had to be dimensioned thicker in order to retain its strength, leading to increasing diameters of the other two gimbal rings. The position of the manipulator attachments, i.e. the outer diameter of the outer gimbal, is fixed, hence the gaps between the rings and the thickness of the two outer rings had to be reduced. This lead to the second change in design. As can be seen in figure 8 the outer gimbal is now completely made out of one part, merging the gimbal ring, the pre-tension brackets and the manipulator attachments, resulting in a stronger and more compact design. To save weight some excess material from the inner gimbal has been removed by drilling holes in radial direction. Also the slider part has been adapted to fit exactly onto the steel rods of the inner gimbal.

The three gimbal rings even as the spring attachments were precision milled from aluminium. The rods are off-the-shelf $\emptyset\ 2\ mm$ silver steel axles lengthened to $25\ mm$. The joints are formed by custom made brass cups and modified set screws. The slider part is realized by modifying an plastic self-lubricating M250 Iglide brushing from Igus (MSM-2026-15), for low friction movement along the rods.

The realized prototype met all requirements stated in section b and weighs only 21 grams. Figures 9 and 10 depict a close-up of the assembled end-effector of respectively the CAD model and the realized prototype.

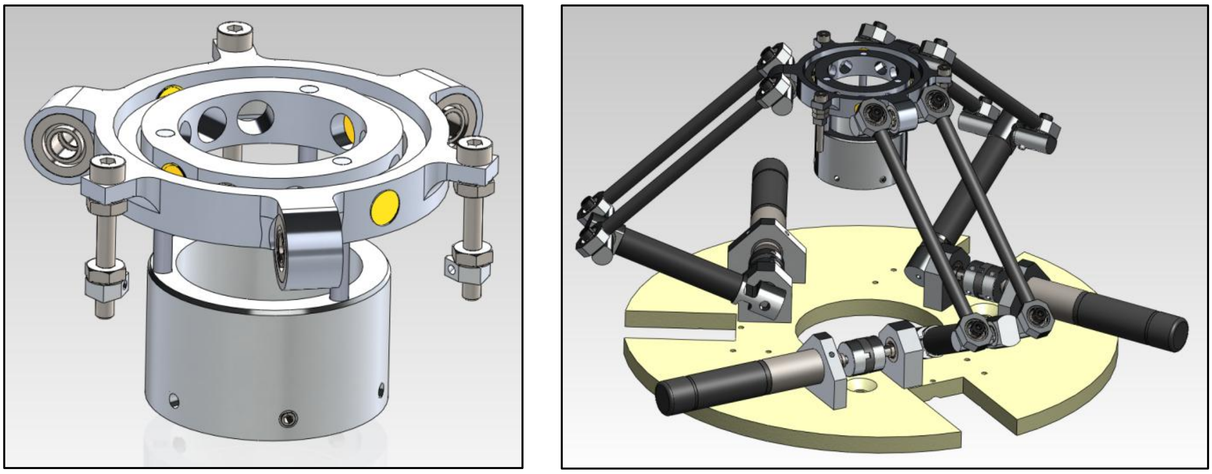

Figure 9: pictures of a CAD assembly of the redesigned end-effector alone (upper) and while assembled to the manipulation system (lower).

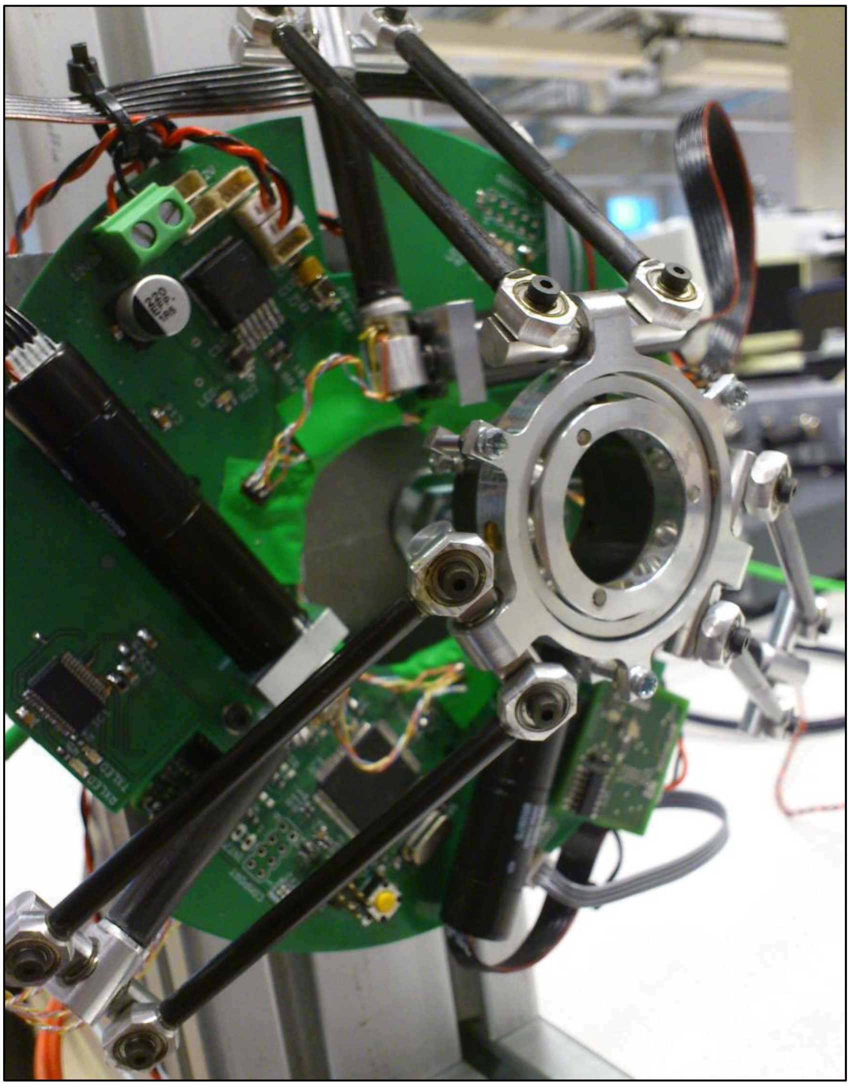

Figure 10: photo of the realized prototype of the end-effector, assembled to the manipulator.

III. NDT-UT sensor module

This section describes the non-destructive testing (NDT) sensor module. The sensor used is a custom made dual crystal ultrasonic testing (UT) sensor with two coaxial plugs. The sensor has a diameter of $20\ mm$ and is $31\ mm$ long. The two plugs protrude another $19\ mm$.

a. Requirements

Compact – The end-effector should not confine the manipulator's workspace of $5 \times 5 \times 5\ cm^3$, hence a compact design is needed.

Compatible – Obviously the NDT module should be compatible with the priorly designed end-effector. This also means that it should be quickly attachable and detachable.

Roll rotation – Besides the 3 DOFs of the end-effector to ensure proper interaction with the inspected surface, an extra rotational DOF is needed to ensure proper measurements. This roll rotation must be actuated and although continuous rotation is not required, it is required to make at least one full rotation.

Robust – The system must be robust in order to survive in-flight collisions while hovering near a structure. Besides the intended contact forces up to approximately 5 N, impact forces up to 20N should be handled without causing damage to the module.

b. Design

The design is shown in figure 11 and consists of very few components. Two rings clamped to the sensor's plugs by M2 set screws and a custom made ring gear, with module 0.3 and 55 teeth, in between. Furthermore a compact Faulhaber motor (0615C4,5S) with compatible 64:1 gearbox is used to actuate the roll rotation via a standard ISO spur gear with module 0.3 and 18 teeth. The inner gear is clamped inside the end-effector slider, hence all other parts of the module, including the motor, rotate along with the sensor. Because continuous rotation was not required this gives no problems concerning wiring to the sensor and motor.

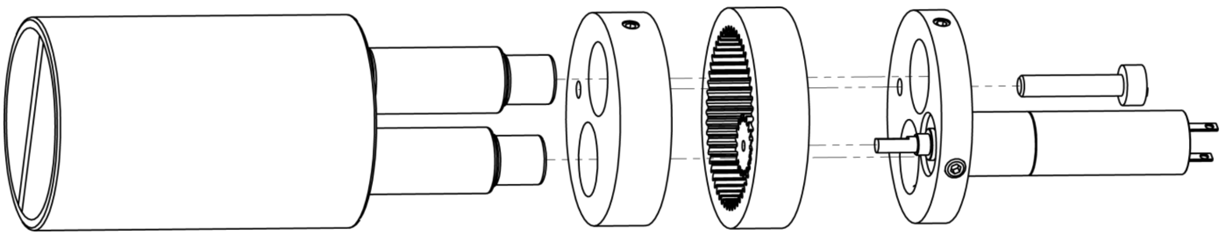

Figure 11: an exploded view of the NDT-UT sensor module, containing from left to right: the NDT sensor, an upper ring with two holes for the sensor's plugs, an inner gear for the actuation, a lower ring with an extra hole to hold the actuator.

c. Realization

The design has been realized and assembled, see figure 12, using several materials and techniques. The two rings on both sides of the gears are made from polyoxymethylene (POM), an excellent precision engineering material with high stiffness and low friction. The custom inner gear is made from machinery steel using electric discharge machining (EDM), also known as spark eroding, an extremely accurate production method, perfectly suited to cut shapes out of hard metal plates. The bolt and set-screws are standard M2 ISO parts. The module, excluding the sensor itself, but including the motor and gearbox, weighs approximately $14\ grams$.

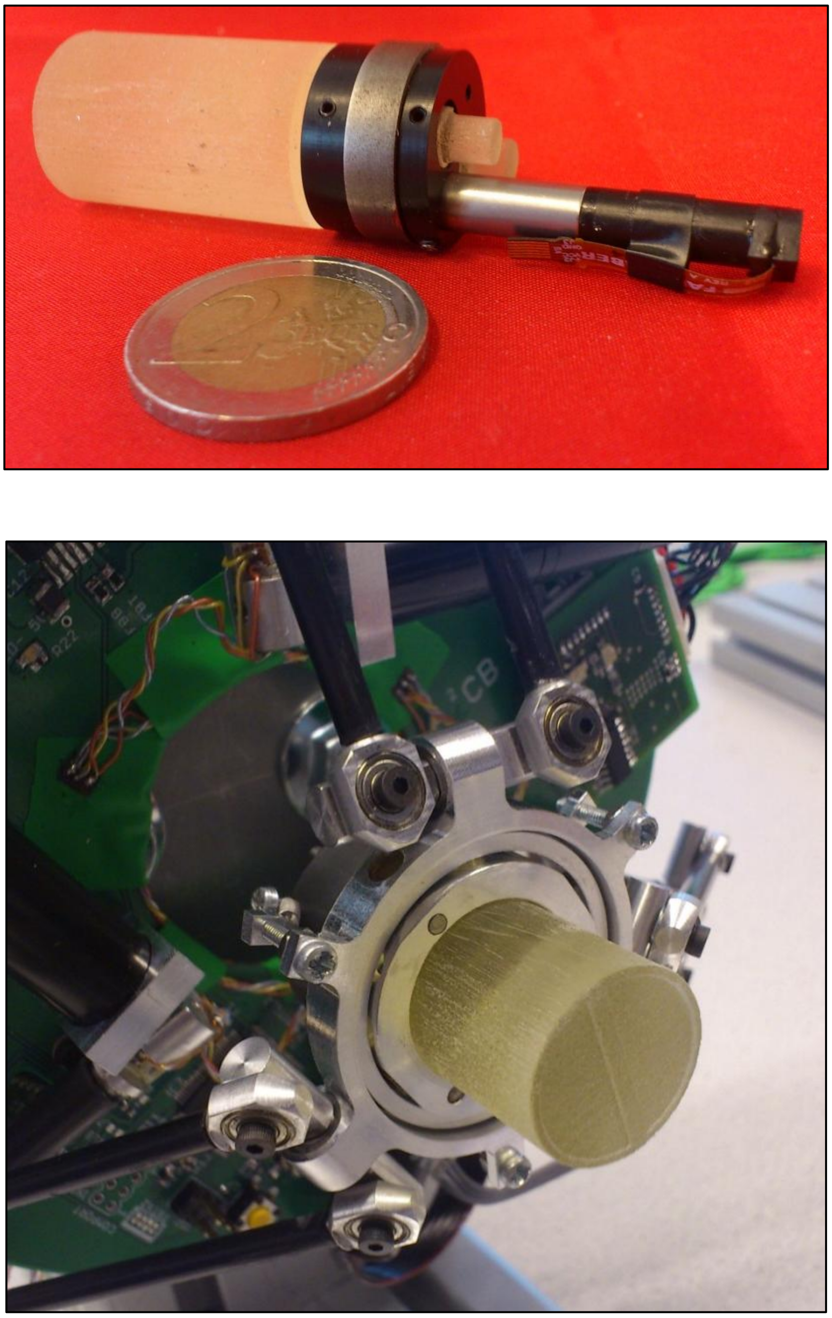

Figure 12: a photo depicting the realized NDT-UT sensor module on its own (upper) and assembled to the manipulator (lower). N.B.: the actual sensor is replaced by a 3D-printed replacement part with exactly the same dimensions.

IV. Gripper module

Equipping the manipulator with a gripper can be useful in various occasions, e.g. object carrying and placement or docking to a structure by grasping a handle or knob. Object carrying by UAVs has recently become a popular research topic and experiments in object lifting [9], cooperative object lifting and group navigation [10] open up a completely new spectrum of possibilities.

In this section an end-effector capable of grasping a variety of objects is elaborated. At first the requirements of this end-effector are listed, followed by a literature study on underactuated gripping devices and variable stiffness actuators. Next a conceptual design is proposed and modeled to investigate the gripper's behavior and the resulting contact forces exerted on an object. The novelty of this gripper lies in the employment of a variable stiffness actuator to gain controllability over the contact force distribution along the phalanges, providing more versatility while maintaining a compact and lightweight design.

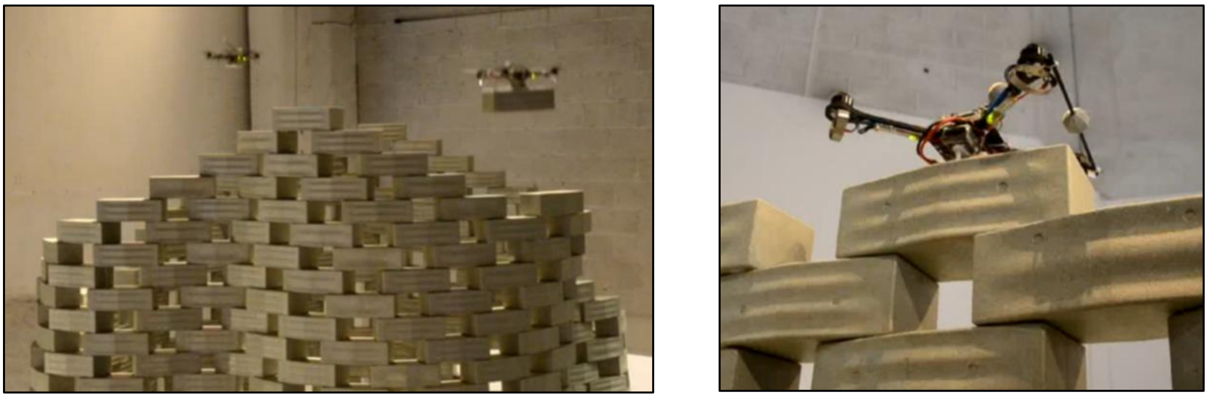

Figure 13: Multiple quadrotors cooperating while building a 6 meter high structure from 1500 prefabricated polystyrene foam modules **[11]**

a. Requirements

Lightweight – A lightweight design is inevitable since the UAV can only generate a limited amount of lift. To maximize the weight of objects that can be grasped and carried, the weight of the gripper itself must be minimalized.

Compact – The gripper should not confine the manipulator's workspace, hence a compact design is needed. Furthermore, the gripper must be compatible with the priorly designed modular end-effector, having an inner diameter of $20\ mm$.

Robust – The gripper must be robust in order to survive in-flight collisions while hovering near a structure. Impact forces up to $20N$ should be handled without causing damage.

Versatile – First of all, the gripper must be capable of grasping a certain range of object sizes. The maximum object size that must be enveloped is a cylinder with a radius of $35\ mm$ (approximately the size of a tennis ball). Secondly the objects geometry might vary. Proper closure around any geometry is needed to ensure stable grasping of arbitrary objects. Thirdly, the gripper must also be versatile with respect to different types of objects. It should be able to firmly grasp a heavy object, as well as a more delicate grasp of a fragile object.

b. Theoretical background

Underactuated grippers

Since usual the actuators are responsible for most of the weight of a grasping device, underactuated robotic fingers are very promising in the development of lightweight and compact grippers while maintaining the ability of form closure around an object to ensure a stable and firm grasp. Since many articles about underactuated gripping devices have been published, this section gives a short summary of the interesting topics for this work.

Several realizations of underactuated fingers have been proposed, however none of these allow controllability of the contact forces applied on the grasped object. S. Krut [12] does show the importance of a specific force profile, in this case isotropic. The three most common concepts are the four bar linkage system [13], pulley tendon system [14] and the monolithic compliant finger [15], all depicted in figure 14. The latter being the mechanically simplest of the three, since it consists of only one component, the pulley tendon system being most promising in realizing compact designs, since actuation is done directly at the phalange's joints and the four bar linkage system being the most robust and adaptable of the three. A disadvantage of the tendon pulley type is that it cannot deliver large grasping forces, thus limiting its versatility. Furthermore, the elasticity of the tendons is known to provide unwanted behaviour.

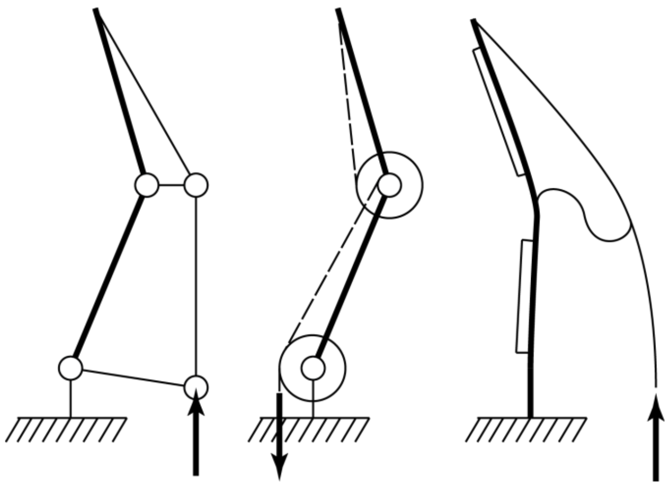

Figure 14: A sketch of three common types of underactuated fingers having 2 phalanges each. From left to right, a four bar linkage, pulley tendon and monolithic compliant finger

To control the behaviour of the multiple degrees of freedom separately several solutions have been proposed. The four bar linkage mechanism is often endowed with (low stiffness) tensional springs supressing all degrees of freedom except the rotation of the proximal phalange. While in free motion the finger behaves as a rigid finger with only one phalange. As soon as the proximal phalange gets in contact with an object, i.e. a contact force builds up at the proximal phalange, the first spring elongates, and the rest of the finger starts enveloping the object (figure 15). Another commonly used solution, especially in the case of pulley tendon based systems, employs joint locks to lock joints up to a certain torque. The closing sequence can be described similarly to the prior case with extension springs, but when re-opening the finger a different situation occurs. In the priorly described case, the stretched extension springs will release their stored energy to automatically open the finger again, whereas the joint locks have no stored energy and need a (negative) actuation torque to reverse the closing process to re-open the finger. In case of the monolithic finger the separate degrees of freedom are completely dependent on the stiffness and contact force distributions along the finger. Since the finger also stores energy when deforming it will also recover to the same state after releasing the actuation torque.

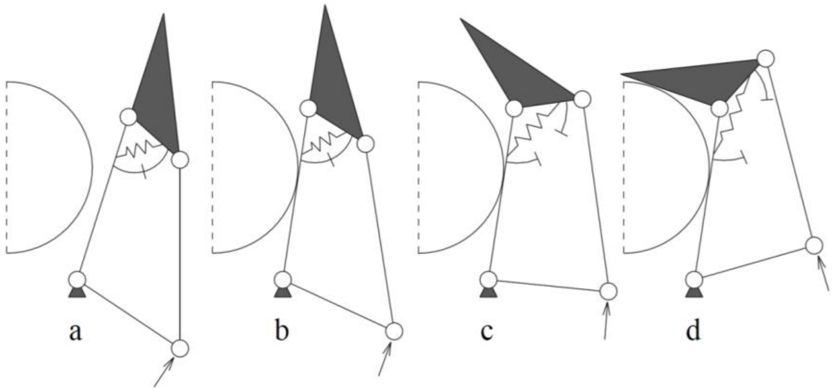

Figure 15: Closing sequence of a (2 DOF) four bar linkage type of underactuated finger.

<u>Variable Stiffness Actuator</u>

Since robots must interact with remote environments or humans more and more frequently, the need for a new actuation mechanism arose. Compliant actuation is the key to stable and safe interaction with unknown environments, and recently many types of Variable Stiffness Actuators (VSAs) have been proposed. A compact and lightweight example is the mini Variable Stiffness Actuator (mVSA) proposed in [16], a device that allows continuous rotation at its output shaft with a stiffness varying from zero to almost infinite.

The basic concept to achieve variable stiffness is a lever arm which is connected to the output shaft on one side and to two pre-tensioned springs on the other side, with a movable pivot point in between (figure 16). The output shaft is connected via a crank shaft mechanism to the right hand side of the lever arm. The mVSA has a layered structure consisting of three stages: 1. the variable stiffness mechanism, 2. the differential mechanism and 3. the actuation stage. The differential layer couples the input from two actuators to the top layer through a transmission matrix, i.e. a certain combination of angular velocities at the input results in a combination of an output rotation and a pivot point translation. The main advantage of such a differential mechanism is that both input torques can be combined at the output shaft, so higher output torques can be generated.

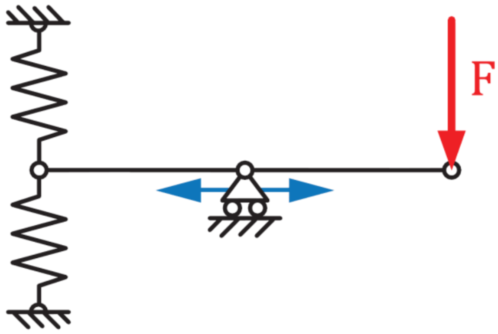

Figure 16: basic concept of the mVSA. One end of the lever arm is connected to springs and the other to the output shaft with a movable pivot point in between.

c. *Model*

To increase the versatility of the gripper, a four bar linkage system is taken, for which the possibility of contact force control through adjusting the spring stiffness is investigated. Especially for grasping fragile objects it is important to know the consequences, in terms of contact forces, of adjustments in actuation torque and spring stiffness. The goal of the model is to find qualitative relations between the input variables, i.e. the actuation torque and the adjustable spring stiffness, and the output variables, i.e. the contact force on the first and second phalange.

Assuming a symmetric planar grasp, a two-dimensional representation is sufficient. Furthermore only static mechanics is concerned, since this analysis provides enough information to reach the goal of this model. In general arbitrary objects should be grasped, but in this analysis only the attitude of the finger is of importance, hence a circular object with radius r_{obj} is assumed to be positioned at the line of symmetry (see figure 17), while touching the palm of the hand. By varying the object radius all attitudes of the finger can be simulated.

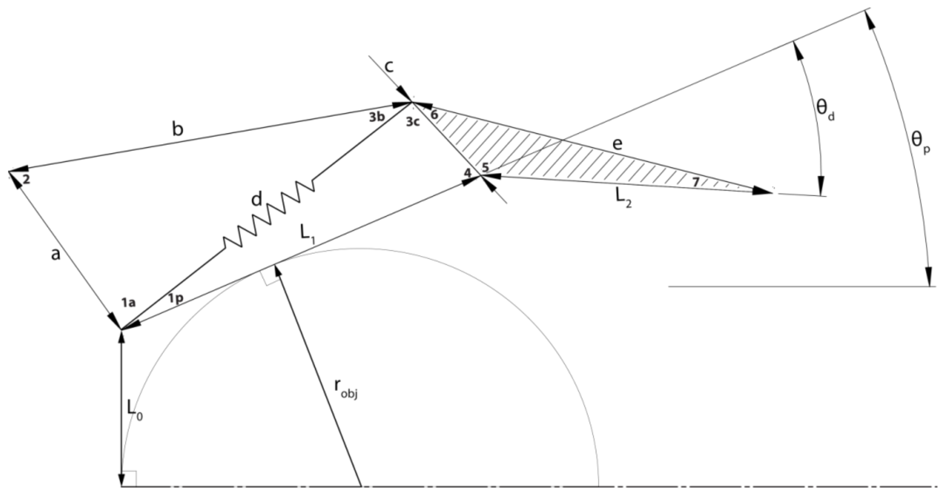

Figure 17: A sketch of the modelled grasping configuration with the object in contact with both the palm and the proximal phalange, fixing $\boldsymbol{\theta_p}$ for a given object size.

Since the angle of the proximal phalange is specified for a given object size due to the contact condition, the finger has only one degree of freedom left, namely the angle of the distal phalange denoted with θ_d. Two situations can still be distinguished: the single contact configuration, in which the distal phalange is not in contact with the object, i.e. contacts solely at the palm and proximal phalange, and the full contact configuration, in which the finger completely envelopes the object so also the distal phalange is in contact. The finger's attitude is completely determined if θ_d is known and this angle can be computed for the single contact case by using static equilibrium equations for the distal phalange, i.e. the sum of moments around the distal joint should equal zero, or from geometry in case of the full contact configuration. Now the finger's attitude is known, the contact forces can be easily calculated from static equilibrium equations. This short description does obviously not cover all the details, for a full description of the model, its derivation and implementation in Matlab please see appendix C.

d. Simulation results

This section describes the results from a simulation of the priorly described model with the following parameters:

$$L_0 = 15.0 \quad L_1 = 30.0 \quad L_2 = 20.8$$
$$a = 10.7 \quad b = 27.0 \quad c = 5.0 \quad \angle 5 = 2.3$$

Figure 18 shows the piecewise linear relations between actuation torque and contact forces. As expected all forces and θ_d start at zero since the spring is at rest in this attitude and no actuation torque is applied. Subsequently the finger starts closing while building up a contact force on the proximal phalange, at a rate independent of the spring stiffness. Note that the torque needed for a certain θ_p does depend on k and so does the torque needed upon which transition to the full contact model takes place. From this transition the slope of F_1 decreases and also the contact force on the distal phalange starts increasing.

Switching the roles of τ_a and k gives the plots displayed in figure 19, where the different lines represent different values of the actuation torque and the stiffness is shown on the x-axis. It can be seen that by increasing the stiffness more than a certain value leads to opening of the finger, hence transitioning to the single contact configuration. From this point increasing the stiffness further does no longer influence the contact forces as was already ascertained from the previous figure.

In general it can be seen that increasing the stiffness leads to an increase of F_1 and a decrease of F_2, thereby shifting the ratio F_2/F_1 towards zero. This contact force ratio (R_{CF}) has an attitude dependent maximum where it will go to for $k \to 0$ or $\tau_a \to \infty$, bounding the theoretical accessible values to:

$$R_{CF} \in [0\,, R_{CF,max}]$$

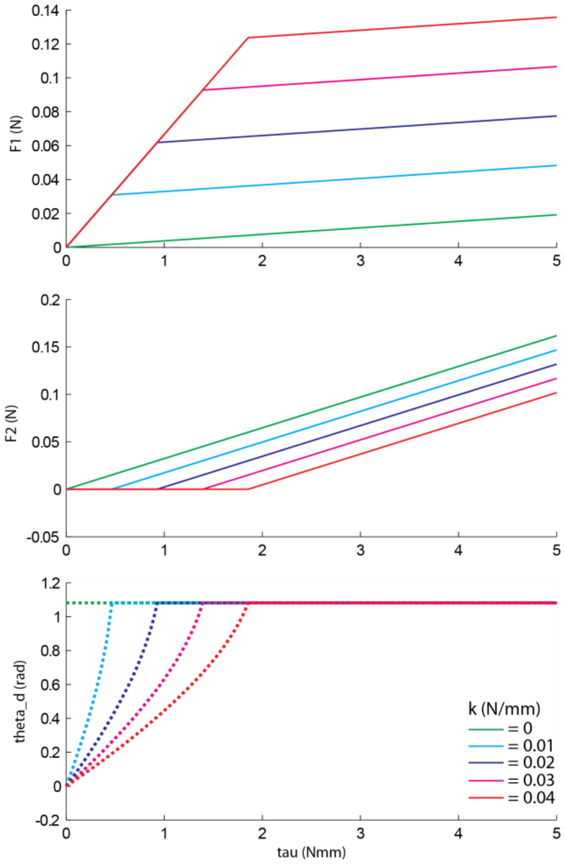

Figure 18: *Plot of respectively* $\boldsymbol{F_1}$, $\boldsymbol{F_2}$ *and* $\boldsymbol{\theta_d}$ *for an increasing actuation torque.* $\boldsymbol{r_{obj} = 25\ mm}$

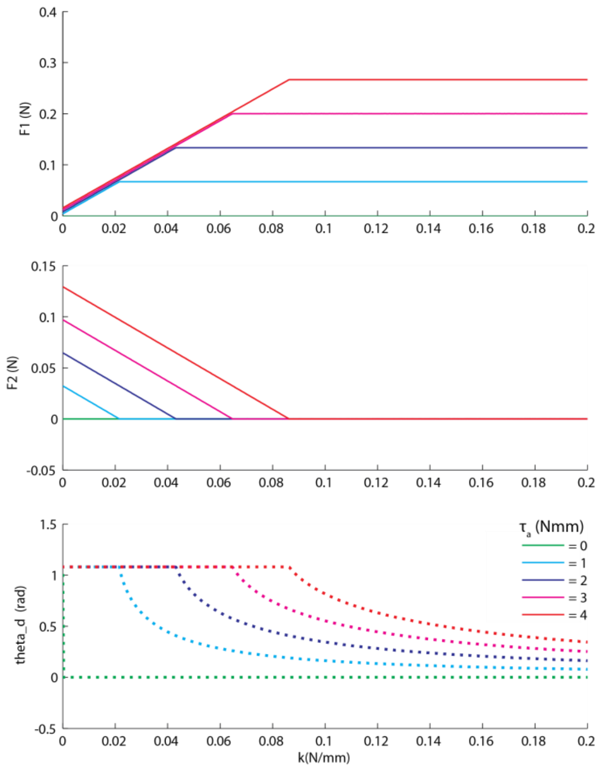

Figure 19: *Plot of respectively* $\boldsymbol{F_1}$, $\boldsymbol{F_2}$ *and* $\boldsymbol{\theta_d}$ *for an increasing spring stiffness.* $\boldsymbol{r_{obj} = 25\ mm}$

When investigating the influence of the object's size and thereby the grasp attitude, only minor differences occur, except for F_1 as function of the torque. The single contact model shows the same results since the finger does not experience a different situation, but for larger objects transition to the full contact model takes place sooner, since the distal phalange will already encounter the object for a smaller closing angle. The full contact configuration on the other hand does show significant change in behavior as can be seen in figure 20. For object radii larger than 27.1 the slope becomes negative leading to configurations with negative contact forces, where this model is obviously no longer valid and a transition to a configuration with contacts solely at the palm and distal phalanges takes place. Figure 21 shows the large variation of the slope of F_1 compared to F_2, which turns out to be almost constant.

Now the influence of all variables (τ_a, k, r_{obj}) on the contact forces is determined, the ratio between the contact forces can be further examined by plotting R_{CF} against both the actuation torque and the spring stiffness for two object sizes (figure 22). First thing to be noticed is the maximum value of R_{CF} that can be reached for a certain object size. It turns out that only for radii larger than 16.7 force isotropy, i.e. $R_{CF} = 1$, can be realized. Furthermore the asymptotic behavior high torque or low stiffness can be observed. These results proof the concept of a compliance controlled underactuated gripper providing controllability over the contact forces in a certain range, however successful implementation requires more research. The model must be expanded to also describe the fingers dynamics and the configuration with contacts solely at the palm and distal phalanges. Furthermore the design parameters can be optimized in order to increase the controllability for a large range of object sizes.

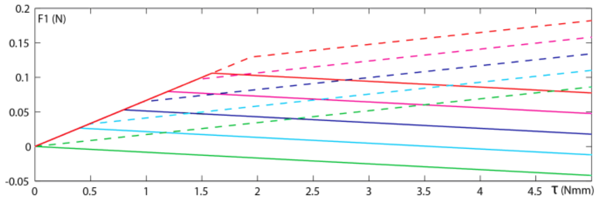

Figure 20: *$\boldsymbol{F_1}$ plotted against the actuation torque for $\boldsymbol{r_{obj} = 20}$ (dashed) and $\boldsymbol{r_{obj} = 35}$ (solid).*

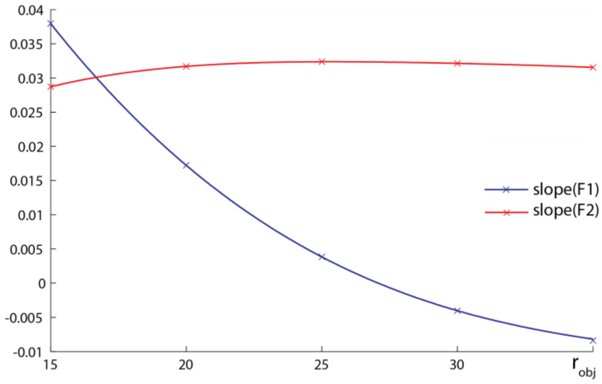

Figure 21: *The slopes of $\boldsymbol{F_1(\tau)}$ and $\boldsymbol{F_2(\tau)}$ plotted against the object size*

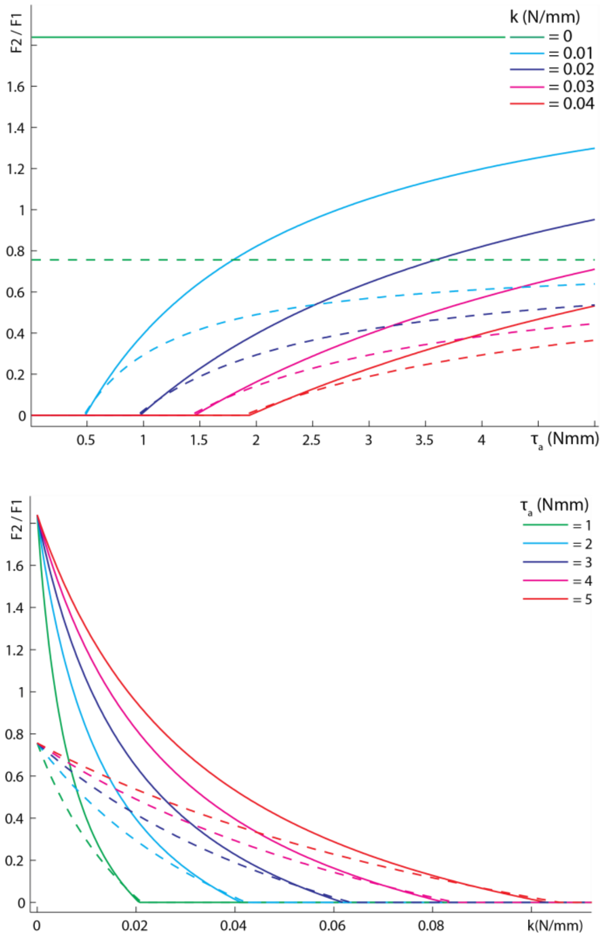

Figure 22: *The contact force ratio $(\boldsymbol{F_2/F_1})$ plotted against respectively the actuation torque and the spring stiffness for $\boldsymbol{r_{obj} = 15}$ (dashed) and $\boldsymbol{r_{obj} = 20}$ (solid)*

e. *Conceptual design*

The four bar linkage mechanism was chosen as a basis because of its robustness and adaptability for a new actuation mechanism. The results from a simple static model show that varying the spring stiffness can be of great use in adjusting the contact forces to the properties of the grasped object. This section proposes a conceptual design in which the mVSA-UT [16] is used to provide both the actuation torque and replace the spring by a controllable variable stiffness.

All dimensions are chosen according to a number of design rules proposed by G.A. Kragten in his PhD thesis on underactuated hands [17]. Starting from a maximum object size that should be enveloped, $r_{obj,max} = 35\,mm$, the lengths of the phalanges can be estimated and from that the other dimensions of the finger were computed. The parts forming the transmission, i.e. the palm, pulley and connecting rods, are dimensioned to form a parallelogram.

The mechanic system consist of many, relatively simple, 3D printed plastic parts connected by off-the-shelf M2 bolts (figure 23). The longer axles are made from a M2 threaded rod, since these lengths were not available as off-the-shelf bolts. By under-dimensioning all hindmost holes many nuts can be omitted, reducing the weight of the overall design.

This prototype is just a preliminary design, hence a redesign will be needed before it can be realized from for instance aluminium, therefore the drawings have not been added to the report. This first prototype is not ready to be implemented as end-effector module, but did give an insight in the dynamics of underactuated grippers.

Figure 23: first 3D-printed prototype of the four bar linkage underactuated gripper.

The gripper will be actuated by a miniaturized variable stiffness actuator as sketched below (figure 24) to gain control over the contact force distribution along the finger. The mVSA is modified to have a double concentric output shaft. The inner shaft is an extension of the compliant output shaft of the mVSA, providing position and stiffness actuation. The outer shaft is internally connected to the top layer's rotating frame, providing merely a non-compliant rotation.

The actuator will placed on the manipulator's baseplate to minimize the weight to be moved around with the end-effector, thereby keeping the disturbances on the UAVs dynamics due to manipulator motion small. Three tendons will run through low-friction, flexible cable guides to the end-effector. Two are needed to connect the actuator's outer shaft to a pulley to actuate the finger bidirectional. The other tendon runs from the inner shaft, through the cable guide, to the distal phalange, thereby replacing the tension spring.

The ratio of the output shaft radii corresponds to the ratio between the radius of the pulley and the distance from the proximal joint to the compliant tendon. This allows the finger to close rigidly in case no object is encountered. When the proximal phalange is in contact with an object the distal phalange can still envelop the object. The torque needed to close the distal phalange now depends on the stiffness imposed by the mVSA.

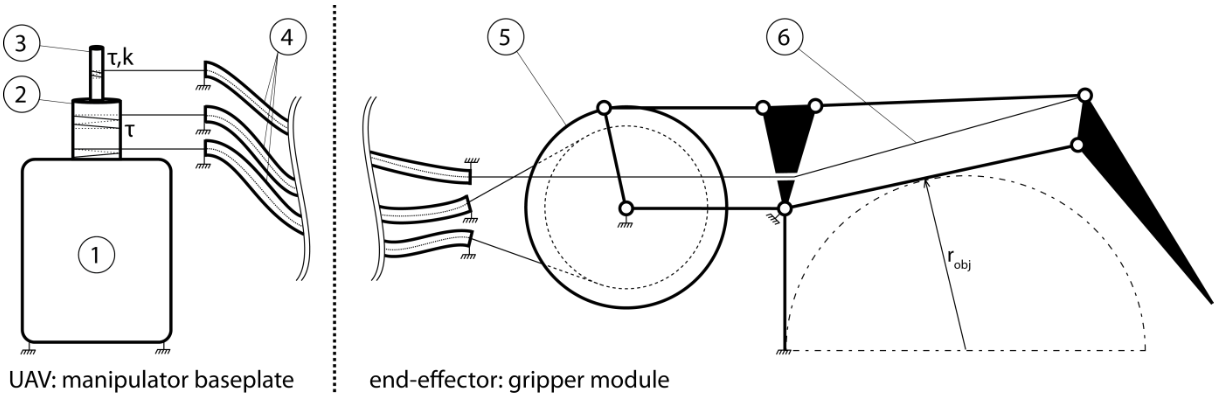

Figure 24: sketch of the implementation of the mVSA to actuate the underactuated finger: 1. mVSA, 2. outer output shaft actuating solely a non-compliant position, 3. compliant output shaft with a controllable stiffness and position, 4. flexible cable guides carrying the tendons to the end-effector, 5. pulley to transform forces from the tendons to a torque actuating the finger, 6. the variable compliant tendon.

f. Recommendations

This design appears to be very promising as the first model already showed, though more work is needed before a working prototype can be realized, which is beyond the timescale of this project. A more detailed model, describing the combined dynamic behaviour of the mVSA, the transmission and the underactuated finger is required to optimize this design. Furthermore the mVSA prototype must be adapted to add the second, non-compliant output shaft. The current mVSA weighs about 100 grams which might be reducible by using lighter materials, e.g. plastics, for the casing. Also the gripper must be redesigned before it can be made of a more durable material, e.g. aluminium or POM. When a prototype of the full system is realized grasping tests and contact force measurements are required to verify the model and the functioning of the prototype.

V. Conclusions and future work

This section summarizes all conclusions from this report and casts a glance on the future perspectives and possible continuations of this project.

First of all, a versatile modular end-effector with 3 passive degrees of freedom was designed and a prototype was realized. The pre-tensionable spring system greatly improved the previous design and the final design consists of fewer parts, resulting in a more compact and lightweight solution.

Secondly a NDT-UT sensor module was proposed and realized. All requirements were met and the result functioned properly. Now the exact dimensions of the slider are known (the inner radius turned out to be slightly larger than designed), the sensor module's dimensions can be slightly adapted to improve the fitting and reduce the play when mounted.

Comparing the old end-effector to the new end-effector carrying the NDT-UT module shows that all improvements did not lead to an increase in weight $\left(m_{ee,1} \approx m_{ee,3} + m_{NDT-UT\ module} \approx 35\ grams\right)$. Furthermore the compactness increased significantly due to the motor placement and the merge of the spring systems.

Thirdly a novel underactuated gripper is proposed. A simple static model showed the usefulness of a controllable stiffness to allow adaptive grasping of different object types. Furthermore a conceptual design employing this controllable stiffness using a variable stiffness actuator is proposed. Due to time constraints this design was not yet examined in further detail. Useful next steps would be the modelling of the complete system, a redesign which is compatible with the end-effector and the realization of the full system.

The development of more task specific end-effector modules would increase the possibilities further. One might think of tasks like for instance brushing, surface cleaning, visual inspection or window cleaning. Most can be realized as very simple and compact modules that can be interchanged quickly to provide maximum profitability.

Besides the development and realization of more modules also the system in general, i.e. the combination of UAV plus manipulator and end-effector, should be improved further. Nowadays flight areas are often surrounded by motion-tracking systems providing accurate measurements to allow autonomous control. Before UAVs can be really implemented autonomously outside a laboratory, better sensoring equipment, for instance stereo vision on board of the UAV, must be implemented.

VI. References

[1] AIRobots [online], http://www.airobots.eu.

[2] W. Fischer, F. Tache and R. Siegwart, „Magnetic wall climbing robot for thin surfaces with specific obstacles," in *Proc. of the Int. Conf. on Field and Service Robotics*, Chamonix, France, 2007.

[3] L. P. Kalra, W. Shen and J. Gu, „A wall climbing robotic system for non-destructive inspecion of above ground tanks," in *IEEE Canadian Conference on Electrical and Computer Engineering (CCECE)*, Ottawa, Canada, 2006.

[4] H. Zhang, J. Zhang, W. Wang, R. Liu and G. Zong, „Sky Cleaner - a real pneumatic climbing robot for glass-wall cleaning," *IEEE Robotic & Automation Magazine,* vol. 13, nr. 1, pp. 32-41, 2006.

[5] H. Yanzeng, S. Hao and W. Yan, „Wall-climbing robot with negative pressure sucker used for cleaning work," *High Technology Letters 5,* pp. 85-88, 1999.

[6] A. Albers, S. Trautmann, T. Howard, T. A. Nguyen, M. Frietsch and C. Sauter, „Semi-autonomous Flying Robot for Physical Interaction with Environment," IEEE conference on Robotics Automation and Mechatronics (RAM), 2010.

[7] M. Fumagalli, „Quadrotor Interacting with a Remote Environment: Control of a Flying Hand".

[8] A. Q. L. Keemink, M. Fumagalli, S. Stramigioli and R. Carloni, „Mechanical Design of a Manipulation System for Unmanned Aerial Vehicles," 2012.

[9] P. Pounds, D. Bersak and A. Dollar, „Grasping From the Air: Hovering Capture and Load Stability," in *IEEE International Conference on Robotics and Automation*, Shanghai, 2011.

[10] D. Melling, M. Shomin, N. Michael and V. Kumar, „Cooperative grasping and transport using multiple quadrotors," in *Proceedings of the International Symposium on Distributed Autonomous Robotic Systems*, 2010.

[11] R. D'Andrea [online], „Flight Assembled Architecture," Dynamic Works (http://raffaello.name/dynamic-works/flight-assembled-architecture) and ETH Zürich (http://www.idsc.ethz.ch/Research_DAndrea/fmec).

[12] S. Krut, „A Force-Isotropic Inderactuated Finger," in *Proc. of the 2005 IEEE International Conference on Robotics and Automation*, Barcelona, Spain, 2005.

[13] T. Laliberté, L. Birglen and C. M. Gosselin, „Underactuation in robotic grasping hands," *Machine Intelligence & Robotic Control,* vol. 4, nr. 3, pp. 1-11, 2002.

[14] R. Pape, „The Effect of Joint Locks in Underactuated Hand Prostheses," Delf, the Netherlands, 2011.

[15] P. Steutel, „Design of a Fully Compliant Under-Actuated Finger with a Monolithic Structure and Distributed Compliance," Delft, the Netherlands, 2010.

[16] M. Fumagalli, E. Barrett, S. Stramigioli and R. Carloni, „The mVSA-UT : a Miniaturized Differential Mechanism for a Continuous Rotational Variable Stiffness Actuator," IEEE International Conference on Biomedical Robotics and Biomechatronics, 2012.

[17] G. A. Kragten, „Dimensional Design," in *Underactuated Hands: Fundamentals, Performance and Design*, TU Delft, 2011, pp. 119-121.

Appendix A – End-effector model

A multipurpose, modular end-effector with three degrees of freedom (DOFs) is modelled to investigate the effects of the spring's pre-tensioning angle on the perceived translational and rotational stiffness. The goal of the spring system is to decouple the translational DOF during impact and provide a stable zero reference angle during free flight.

a. Definitions and assumptions

The model can be simplified without reducing its usefulness by choosing for a two dimensional representation of the end-effector. The three circularly spaced springs are represented by two springs on the lower and upper side of the end-effector, both pre-tensionable at an angle α that lies between 0 and 90°.

The complete configuration is sketched in figure 25, where the upper and lower spring are denoted with respectively subscript 1 and 2, α_i is the pre-tensioning angle, $x_{pt,i}$ is the pre-tensioning distance in millimetres and gravity acting in downward direction. Note that that the translational displacement of the end-effector (x), is not given in the inertial frame, but along an axis in the end-effector's reference frame.

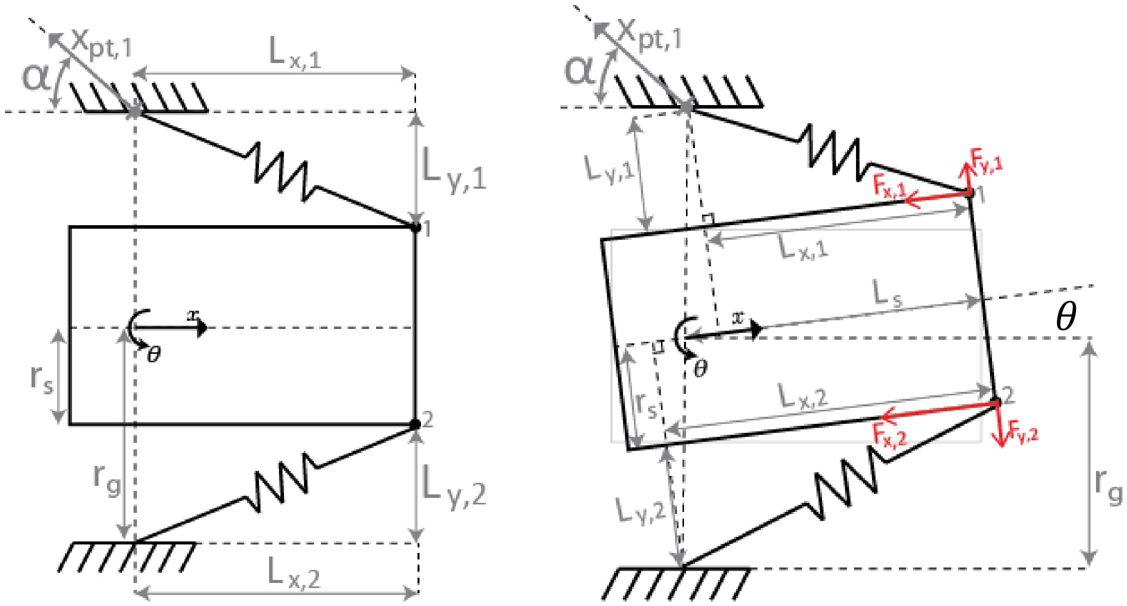

Figure 25: a sketch of the two-dimensional representation of the end-effector in both its neutral (left) and rotated position (right). All important variables are denoted, including the two DOFs: $\boldsymbol{\theta}$ and $\boldsymbol{x}$.

A relatively simple static model is sufficient to reach the goal of this model. This means inertial forces are not taken into account. Furthermore (static) friction is neglected and the used springs are linear and at rest when the end-effector is in its neutral position. At last the end-effector is assumed to be completely rigid, having two degrees of freedom: a translation along its longitudinal axis and a rotation around an axis perpendicular to the plane, centred and at a distance $L_s + x$ from its right end. The range of motion is confined by mechanical limitations to: $x \in [0,10]\ mm$ and $\theta \in [-30,30]°$.

b. Static model

The goal of the model is finding the stiffness perceived at both the translational and the rotational DOF, i.e. what are the resulting force and moment for a certain translation and rotation Since the springs are linear, superposition allows great simplification of the model. Instead of expressing the spring's force in the actual length of the spring and subsequently decomposing this force in the components $F_{x,i}$ and $F_{y,i}$, we can directly relate both components of the force directly to the components in x and y direction of the total elongation:

1. $$F_{x,i} = k_i\left(l_{x,i} - l_s\right)$$

2. $$F_{y,i} = k_i\left(l_{y,i} - r_g + r_s\right)$$

The length of the springs depend on both the translation and the rotation of the end-effector. From the rotated geometry sketch the following equations can be derived:

3. $$l_{x1} = l_s - r_g \sin(\theta) + x + x_{pt,1} \cos(\alpha + \theta)$$

4. $$l_{x2} = l_s + r_g \sin(\theta) + x + x_{pt,2} \cos(\alpha - \theta)$$

5. $$l_{y1} = r_g \cos(\theta) - r_s + x_{pt,1} \sin(\theta + \alpha)$$

6. $$l_{y2} = r_g \cos(\theta) - r_s + x_{pt,2} \sin(-\theta + \alpha)$$

The resulting force in x-direction (F_x) and moment around the centre of rotation (M) are given by:

7. $$F_x \quad = F_{x,1} + F_{x,2}$$

8. $$M_{cr} = (F_{x2} - F_{x1}) \cdot r_s + \left(F_{y2} - F_{y1}\right) \cdot (l_s + x)$$

After substitution of equations $1 - 6$ and rearrangement of the results, the expressions yield respectively:

9. $$F_x \quad = (k_1 + k_2)x + (k_2 - k_1)r_g\, sin(\theta) + (p_1 + p_2)\, cos(\theta + \alpha)$$

10. $$M_{cr} = (k_1 + k_2) \cdot r_s r_g\, sin(\theta) + (k_2 - k_1) \cdot \left[r_s x + r_g(l_s + x) \cdot (cos(\theta) - 1)\right] + (p_2 - p_1) \cdot [r_s\, cos(\theta + \alpha) + (l_s + x)\, sin(\theta + \alpha)]$$

The variables $p_1$and p_2 are the pre-tensioning forces, i.e. $p_i = x_{pt,i} \cdot k_i$ and are introduced because of compactness.

For the end-effector's zero reference position, i.e. $\theta = 0$ and $x = 0$, it can be seen that F_x and M_{cr} reduce to:

11. $$F_x(\theta = 0, x = 0) = (p_1 + p_2)\, cos(\alpha)$$

12. $$M_{cr}(\theta = 0, x = 0) = (p_2 - p_1) \cdot [r_s\, cos(\alpha) + l_s\, sin(\alpha)]$$

Especially this second expression (equation 12) is of importance, since a certain torque is needed to maintain this zero reference position despite gravity. It turns out that α is of great influence on the maximal moment that can be generated by pre-tensioning the springs. It turns out that for any value of α in its range $\{0,90\}°$ the contribution to the total moment is positive, but for certain values for r_s and l_s, there will be a maximum on this interval, that is worth investigating.

The stiffnesses, k_x and k_{th}, can now also be computed by differentiating equations 9 and 10 to x and θ respectively:

13. $$k_x = \frac{\partial}{\partial x} F_x = k_1 + k_2$$

14. $$k_\theta = \frac{\partial}{\partial \theta} M_{cr} = (k_1 + k_2) \cdot r_s r_g \cos(\theta) - (k_2 - k_1) \cdot r_g (ls + x) \cdot \sin(\theta) + (p_2 - p_1) \cdot [(l_s + x) \cdot cos(\theta + \alpha) - r_s \cdot sin(\theta + \alpha)]$$

Note that these stiffnesses are merely two of the four components of the stiffness matrix describing the full two-dimensional situation:

15. $$\begin{Bmatrix} F_x \\ M_{cr} \end{Bmatrix} = \begin{bmatrix} k_x & k_1 \\ k_2 & k_\theta \end{bmatrix} \begin{Bmatrix} dx \\ d\theta \end{Bmatrix}$$

Where k_1 and k_2 are terms relating the force in x-direction to the displacement in θ-direction and vice versa. These cross terms are not of importance to the rest of the modelling and hence are not worked out, but can be computed, for completeness, by differentiating equation 9 with respect to θ and equation 10 with respect to x.

Let us now take a look at what we have achieved so far, to see whether we can get a feeling for what is going on. The perceived translational stiffness, k_x, turns out to be constant, i.e. independent of the rotation of the end-effector, the pre-tensioning angle and the amount of pre-tensioning. Of course this does not imply that pre-tensioning is useless, since the force is still influenced by the pre-tensioning distance and angle, it only says that, no matter in which position and pre-tension configuration the end-effector is, the force needed for a displacement of 1 mm is $(k_1 + k_2)\ N$.

The perceived rotational stiffness, k_θ, is slightly more complex and certainly not constant for all configurations. Expression 14 can be simplified by assuming θ small and taking the first term of the sine and cosine Taylor series, i.e. $\cos(\theta) \approx 1$ and $\sin(\theta) \approx \theta$, which is a pretty good approximation since $\theta \in [-30°, 30°]$. Furthermore we take $k_1 = k_2 = k$ for the moment, so both springs used are have the same stiffness. This results in the following, greatly simplified, equation for k_θ:

16. $$k_\theta \approx 2k r_s r_g + k\left(x_{pt,2} - x_{pt,1}\right) \cdot [(l_s + x) \cdot cos(\theta + \alpha) - r_s \cdot sin(\theta + \alpha)]$$

In a first order approximation the rotational stiffness comprises a constant term, related to the sum of the individual stiffnessess similarly to the translational part, and a term dealing with the pre-tensioning applied.

Appendix B – End-effector prototype technical drawings

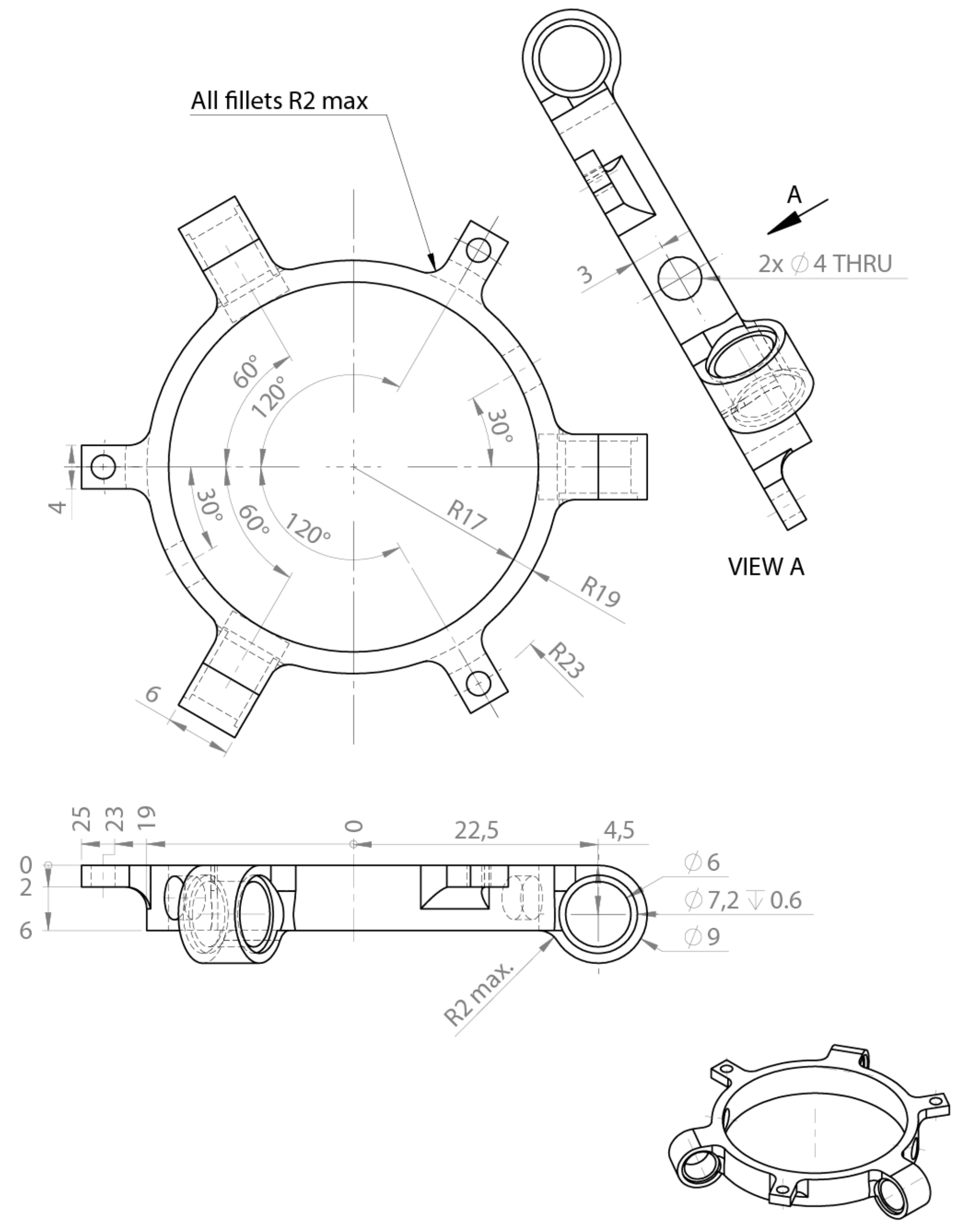

PROJECTION METHOD	UNLESS STATED OTHERWISE: TOLERANCES ± 0,1 MM	DRAWN	--	DATE	2-4-2012
		CHECKED	--	SCALE	2:1
UNIVERSITEIT TWENTE.	MATERIAL -- --	TITLE Part 1: Outer Gimbal		REV. 01	
	SURFACE FINISH --	DRAWING NO. -- FILE / PART NAME 1_EE_gimbal_outer_new		A4	
FACULTY OF ENGINEERING	DIMENSIONS IN MILLIMETERS			SHEET 1 OF 1	

TAG	X LOC	Y LOC	SIZE	Tolerance
1	-5,80	-10,046	∅ 2.1	⌖ 0.02
2	-5,80	10,046	∅ 2.1	⌖ 0.02
3	11,600	0	∅ 2.1	⌖ 0.02

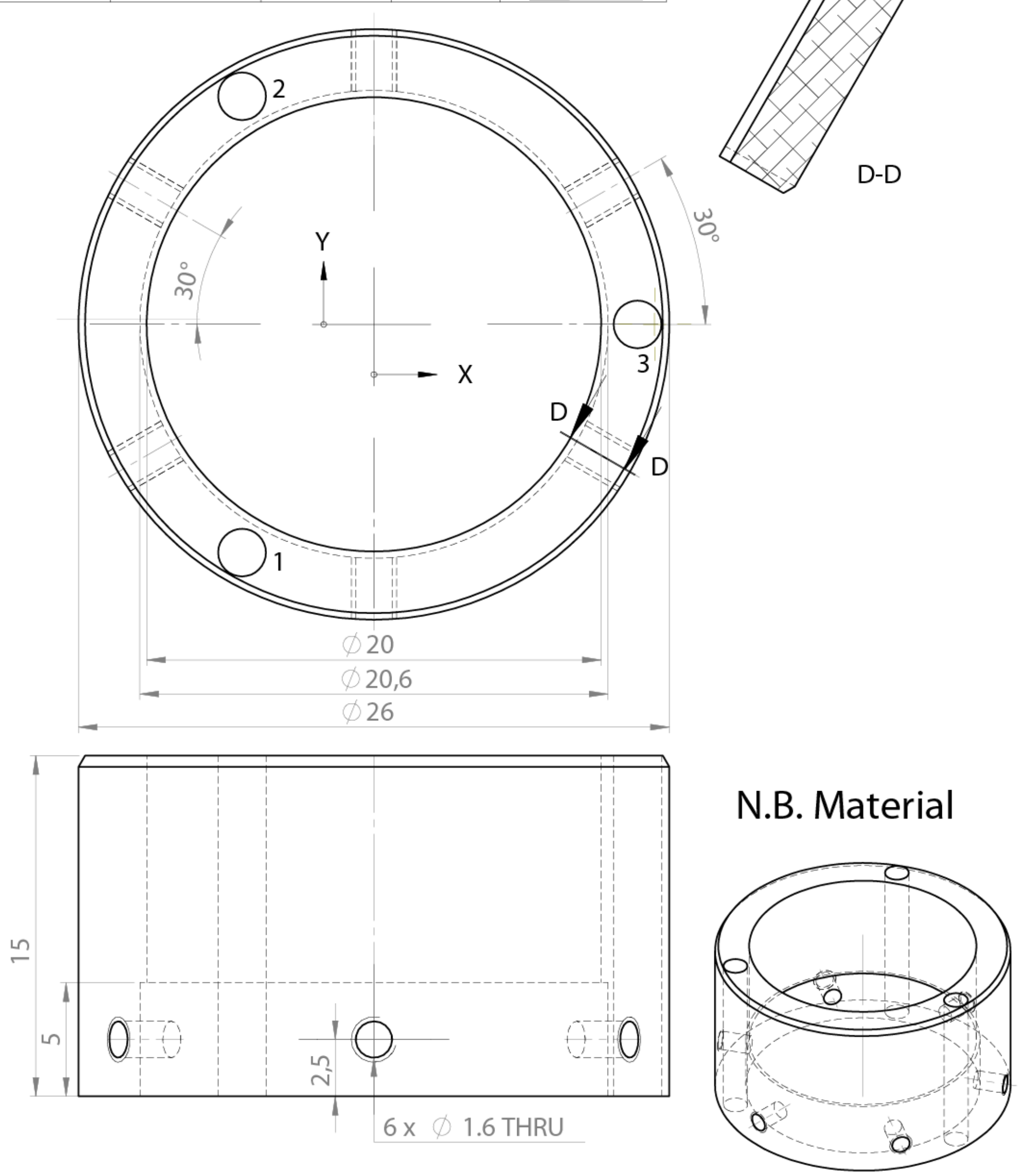

PROJECTION METHOD

UNLESS STATED OTHERWISE:
TOLERANCES ± 0,1 MM

DRAWN	--	DATE	2-4-2012
CHECKED	--	SCALE	4:1

UNIVERSITEIT TWENTE.

FACULTY OF ENGINEERING

MATERIAL
Igus: Iglide-M250
MSM-2026-15

SURFACE FINISH
--

TITLE
Part 20: Slider

REV.
01

DRAWING NO.
--

FILE / PART NAME
20_EE_slider_new

A4

DIMENSIONS IN MILLIMETERS

SHEET 1 OF 1

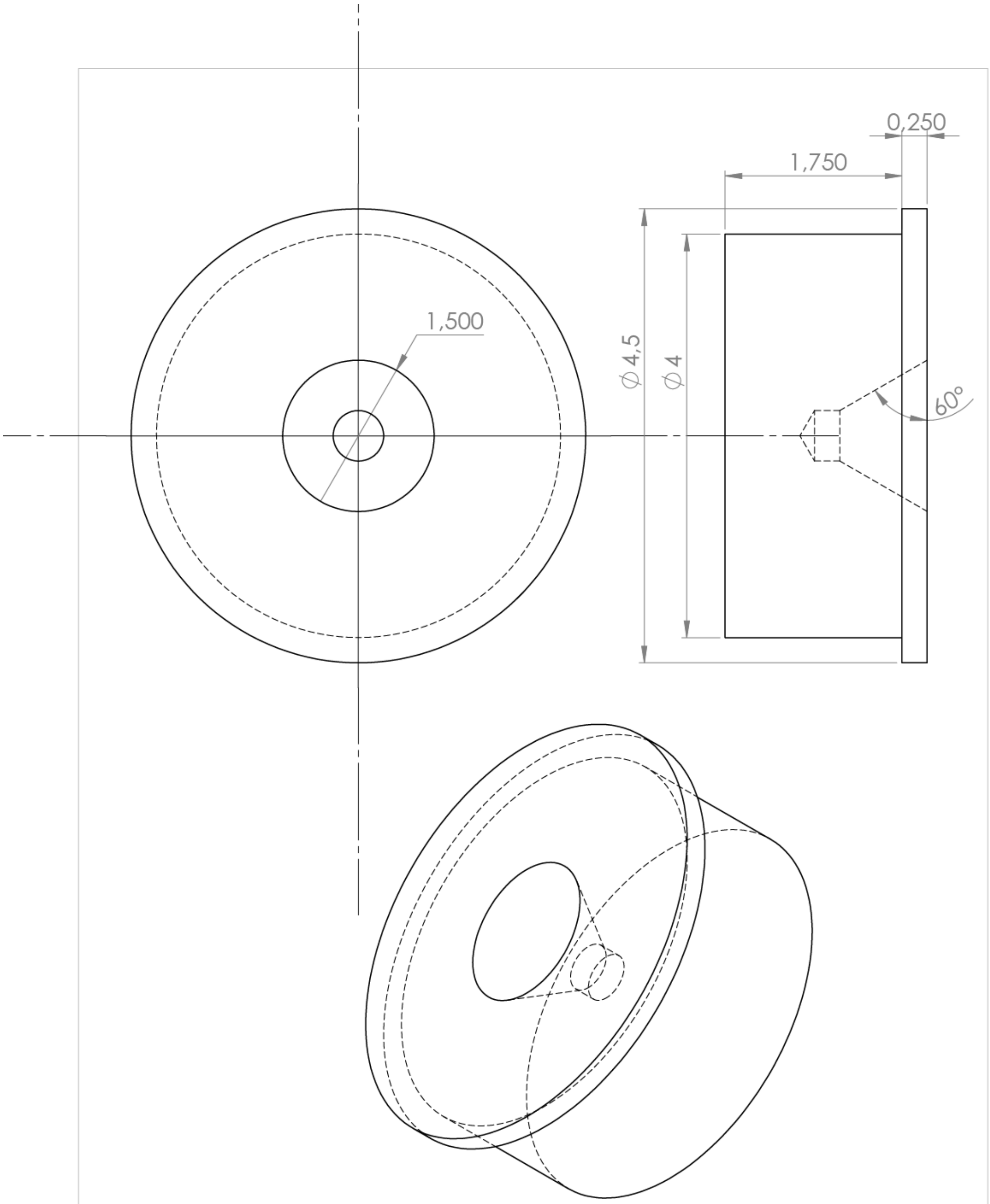

PROJECTION METHOD	UNLESS STATED OTHERWISE: TOLERANCES ± 0,1 MM	DRAWN	--	DATE	19-3-2012
		CHECKED	--	SCALE	20:1

UNIVERSITEIT TWENTE.	MATERIAL Brass?? --	TITLE Cardan Joint	REV. 01
		DRAWING NO. --	
	SURFACE FINISH --	FILE / PART NAME 11_Cardan_Joint_Cup	A4
FACULTY OF ENGINEERING	DIMENSIONS IN MILLIMETERS	SHEET 1 OF 1	

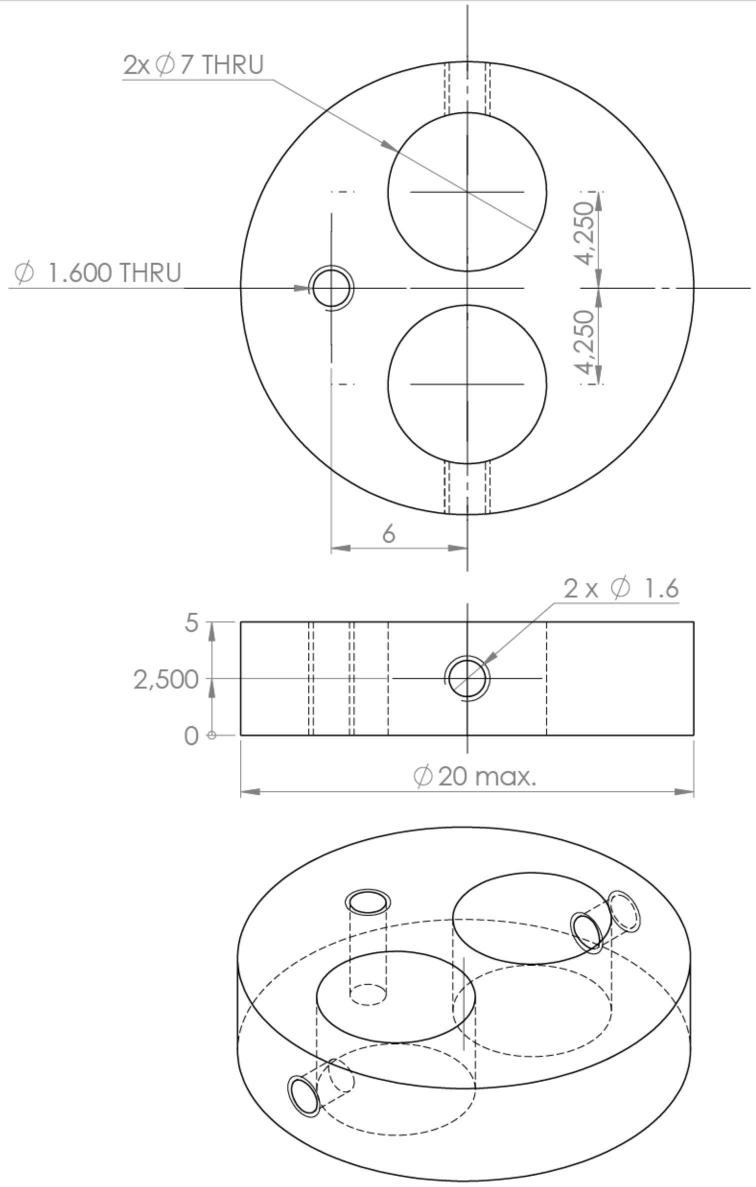

PROJECTION METHOD	UNLESS STATED OTHERWISE: TOLERANCES ± 0,1 MM	DRAWN	--	DATE	15-3-2012
		CHECKED	--	SCALE	4:1

UNIVERSITEIT TWENTE.	MATERIAL -- --	TITLE Slider Ring Upper	REV. 01
		DRAWING NO. --	
	SURFACE FINISH --	FILE / PART NAME 10_EE_slider_ring_upper	A4
FACULTY OF ENGINEERING	DIMENSIONS IN MILLIMETERS	SHEET 1 OF 1	

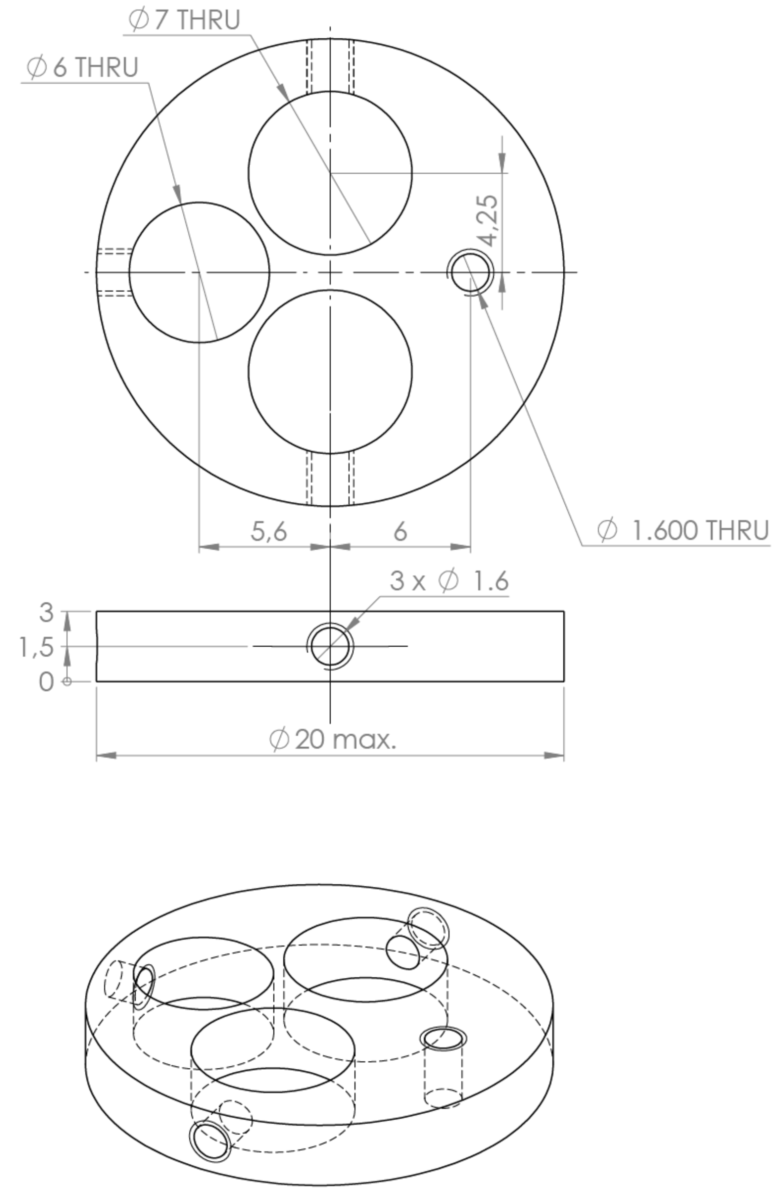

PROJECTION METHOD	UNLESS STATED OTHERWISE: TOLERANCES ± 0,1 MM	DRAWN	--	DATE	13-3-2012
		CHECKED	--	SCALE	4:1
UNIVERSITEIT TWENTE.	MATERIAL -- --	TITLE Slider Ring Lower		REV.	01
		DRAWING NO. --			
	SURFACE FINISH --	FILE / PART NAME 9_EE_slider_ring_lower			A4
FACULTY OF ENGINEERING	DIMENSIONS IN MILLIMETERS			SHEET 1 OF 1	

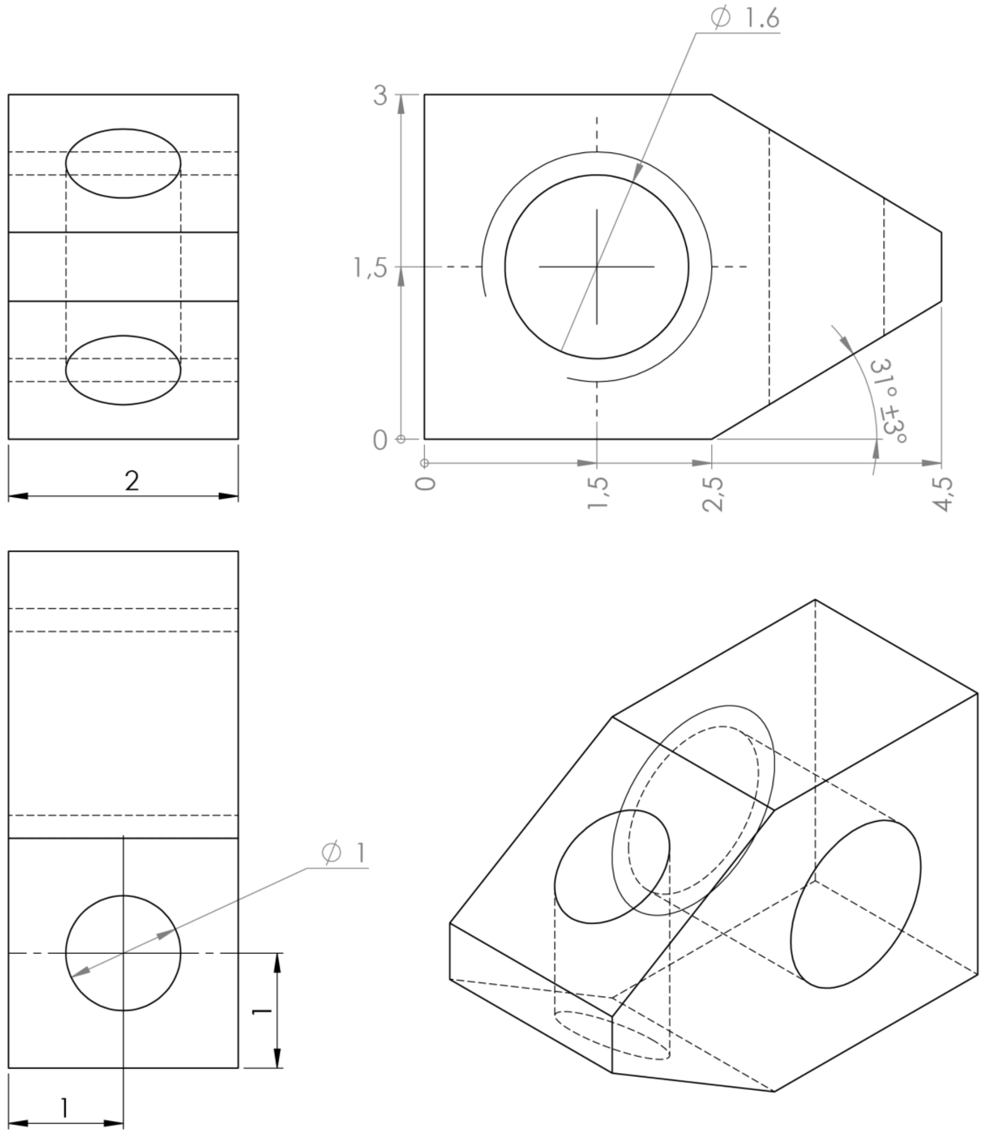

PROJECTION METHOD	UNLESS STATED OTHERWISE: TOLERANCES ± 0,1 MM	DRAWN	--	DATE	13-3-2012
		CHECKED	--	SCALE	20:1
UNIVERSITEIT TWENTE.	MATERIAL -- --	TITLE Spring Pre-loader		REV. 01	
		DRAWING NO. --			
	SURFACE FINISH --	FILE / PART NAME 5_EE_Spring_preloader		A4	
FACULTY OF ENGINEERING	DIMENSIONS IN MILLIMETERS			SHEET 1 OF 1	

TAG	X LOC	Y LOC	SIZE	Position Tolerance
1	-10,046	-5,80	∅ 2 H7	⌖ 0.02
2	0	11,600	∅ 2 H7	⌖ 0.02
3	10,046	-5,80	∅ 2 H7	⌖ 0.02

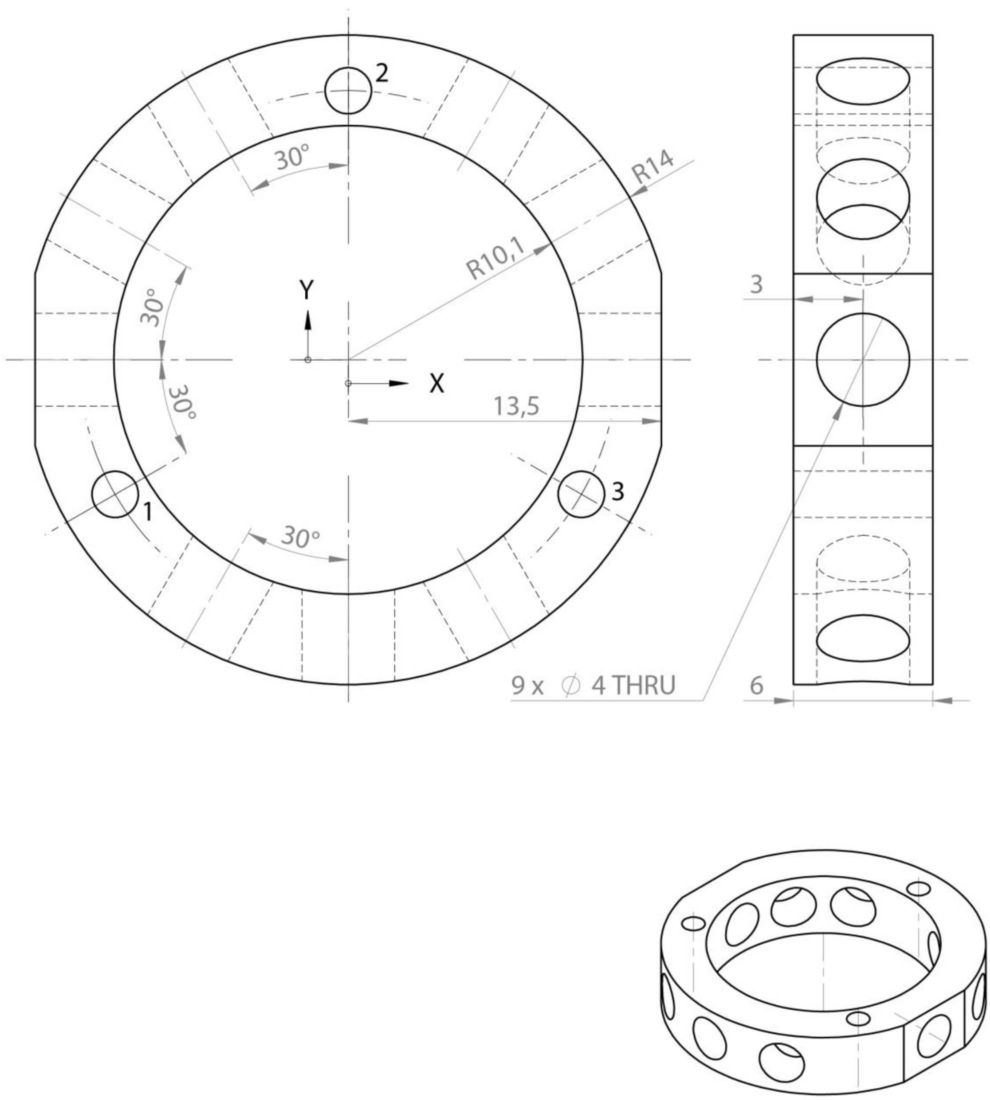

PROJECTION METHOD	UNLESS STATED OTHERWISE: TOLERANCES ± 0,1 MM	DRAWN	--	DATE	2-4-2012
		CHECKED	--	SCALE	4:1

UNIVERSITEIT TWENTE.	MATERIAL -- --	TITLE Part 3: Inner Gimbal	REV. 01
		DRAWING NO. --	
	SURFACE FINISH --	FILE / PART NAME 3_EE_gimbal_inner_new	A4
FACULTY OF ENGINEERING	DIMENSIONS IN MILLIMETERS		SHEET 1 OF 1

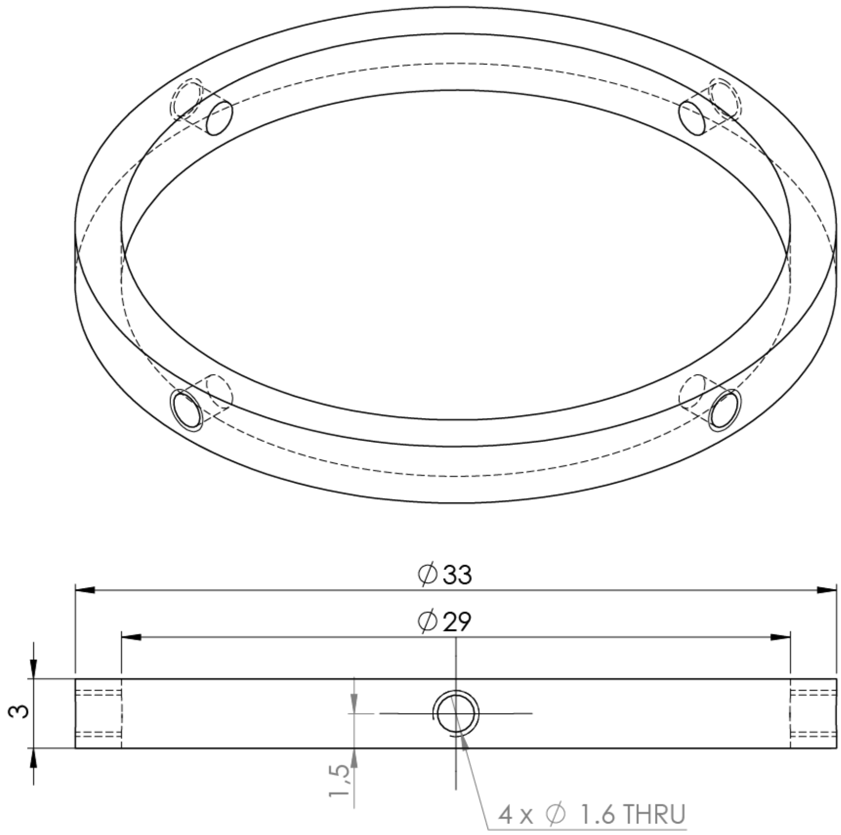

PROJECTION METHOD	UNLESS STATED OTHERWISE: TOLERANCES ± 0,1 MM	DRAWN	--	DATE	13-3-2012
		CHECKED	--	SCALE	4:1
UNIVERSITEIT TWENTE.	MATERIAL -- --	TITLE Part 2: Middle Gimbal		REV. 01	
	SURFACE FINISH --	DRAWING NO. --		A4	
		FILE / PART NAME 2_EE_gimbal_middle_new			
FACULTY OF ENGINEERING	DIMENSIONS IN MILLIMETERS			SHEET 1 OF 1	

Appendix C – gripper model

An underactuated four bar linkage finger is modeled to investigate the use of a variable compliance in order to be able to control the contact forces exerted on the grasped object. The geometry is sketched below, naming all angles and lengths used. First the kinematic modeling will be described, followed by two static models describing respectively the situations in which both phalanges are in contact and in which only the proximal phalange is in contact with the object. Then both models are merged to describe the contact forces for a given compliance while increasing the actuation torque and the possibility of contact force control through controlling the compliance of the spring can be investigated.

a. Definitions and assumptions

The palm of the gripper (L_0) is defined to be fixed, all bars are assumed completely rigid and all joints are assumed to be perfect, frictionless joints. Furthermore gravitational forces are not taken into account, assuming the finger to be in horizontal position. Since the model describes static behavior also inertial forces are not taken into account. Furthermore the contact forces are assumed to be perpendicular to the phalange, neglecting frictional forces between both surfaces. Unless otherwise specified all angles are in radians, distances in millimeters and forces in Newton. At last the range of motion is constrained:

1) $\theta_d \in [\,0\,,2\,]$ and $\theta_p \in [-1.5\,,1.5]$

b. Kinematic model

The finger has two degrees of freedom (DOFs) named θ_p and θ_d corresponding to the opening angle of proximal and distal phalange respectively. The opening angle of the proximal phalange does not change the geometry of the finger and therefore does not influence the contact forces in static equilibrium. An fixed circular object with radius r_{obj} is placed on the grippers symmetry line so that it is in contact with both the palm and the proximal phalange, thereby defining the opening angle of the proximal phalange:

2) $\theta_p = 2 \cdot \tan^{-1}\left(\frac{r_{obj}}{L_0}\right) - \frac{\pi}{2}$

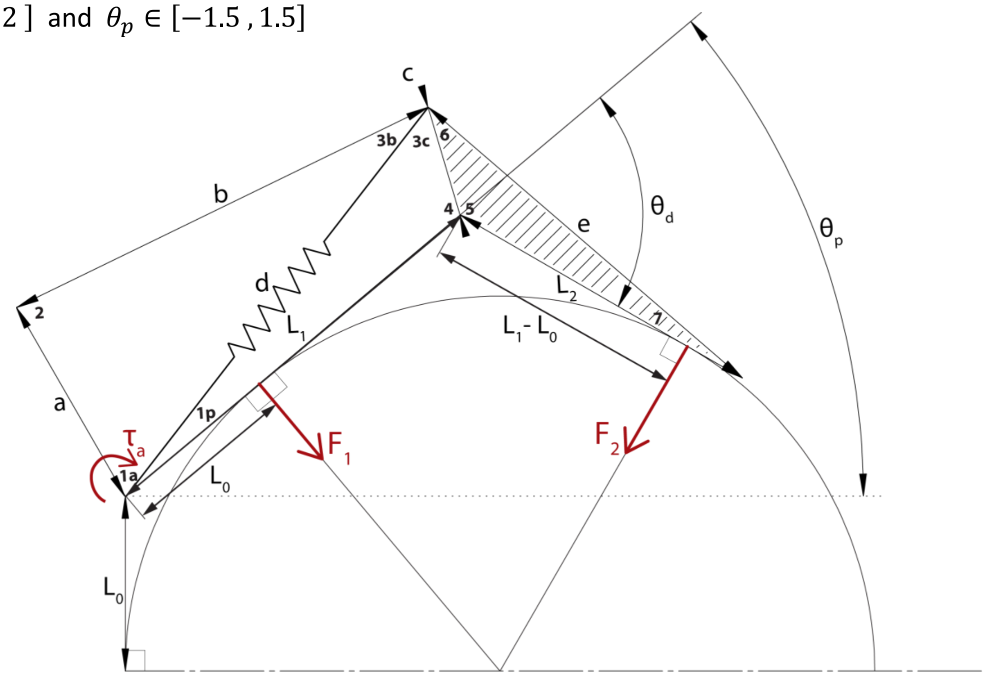

Figure 26: *Sketch defining the model's parameters. Note that besides angles 1 to 4 also the length of the spring, depends on* $\boldsymbol{\theta_d}$

By fixing one DOF all variable parameters can now be expressed in the remaining one, the opening angle of the distal phalange, using simple geometric relations and the rule of cosines, a very useful expansion of Pythagoras theorem, repetitively.

3) $\angle 4 = \pi - \angle 5 + \theta_d$

4) $d = \sqrt{L_1^2 + c^2 - 2 \cdot L_1 \cdot c \cdot \cos(\angle 4)}$

5) $\angle 2 = \cos^{-1}\left(\frac{a^2+b^2-d^2}{2 \cdot a \cdot b}\right)$

6) $\angle 1_p = \cos^{-1}\left(\frac{{L_1}^2+d^2-c^2}{2 \cdot L_1 \cdot d}\right)$

7) $\angle 1_a = \cos^{-1}\left(\frac{a^2+d^2-b^2}{2 \cdot a \cdot d}\right)$

8) $\angle 3_b = \cos^{-1}\left(\frac{b^2+d^2-a^2}{2 \cdot b \cdot d}\right)$

9) $\angle 3_c = \cos^{-1}\left(\frac{c^2+d^2-L_1^2}{2 \cdot c \cdot d}\right)$

Logically $\angle 1$ and $\angle 3$ are defined as the sum of the corresponding subangles.

c. Static model

The static modeling is done by writing moment and force equilibriums for all components. Since all parts should be at rest the sums of efforts should equal zero for every part. The free body diagrams of the separated parts denoting all forces and moments used can be found in figure 27. Beam b is not shown since it only transmits a force in its longitudinal direction from beam a to the distal phalange. All moments are defined positive in clockwise direction.

Full contact

In case both phalanges are in contact with the object the attitude of the finger is predefined and the angle of the distal phalange is given by:

10) $\theta_d = \pi - 2 \cdot \tan^{-1}\left(\frac{r_{obj}}{L_1 - L_0}\right)$

Summing moments on the transmission beam around the proximal joint (pj) gives a relation between F_a and the actuation torque:

11) $\sum M_{pj} = \tau_a - F_a \cdot a \cdot \sin(\angle 2) = 0$

The resulting moment on the distal phalange around the distal joint (dj) should also equal zero, providing an expression from which F_2 can be computed:

12) $\sum M_{dj} = F_a \cdot c \cdot \sin(\angle 3) - F_S \cdot c \cdot \sin(\angle 3_c) - F_2 \cdot (L_1 - L_0) = 0$

Where F_S is the force caused by the spring, depending on the spring stiffness (k) and elongation, where for the rest of the model the spring is defined to be at rest for $\theta_d = 0$, i.e. $L_{S0} = d(\theta_d = 0)$:

13) $F_S = k \cdot (d - L_{S0})$

To find F_1, first reaction forces $F_{r,x}$ and $F_{r,y}$

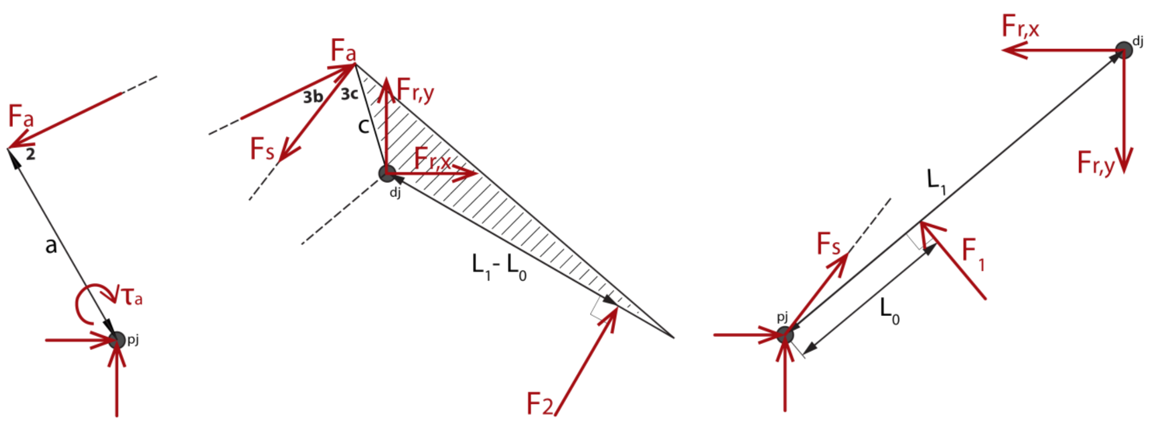

Figure 27: *Free body diagrams of respectively the transmission beam* $(\boldsymbol{a})$*, the distal* $(\boldsymbol{L_2})$ *and the proximal phalange* $(\boldsymbol{L_1})$ *All forces required for the model are named, the other (reaction) forces are left blank*

must be obtained, which is done through force equilibrium in both x and y direction of the distal phalange:

14) $\begin{Bmatrix} F_{r,x} \\ F_{r,y} \end{Bmatrix} + \sum_i F_i \cdot \begin{Bmatrix} \cos(\alpha_i) \\ \sin(\alpha_i) \end{Bmatrix} = 0$

With α_i the angle between the force vector and the positive x-axis:

15) $$\begin{aligned} \alpha_a &= \theta_p + \angle 1 + \angle 2 + \pi \\ \alpha_s &= \theta_p + \angle 1_p + \pi \\ \alpha_2 &= \theta_p - \theta_d + \pi/2 \end{aligned}$$

Now the reaction force on the proximal phalange (F_1) can be computed from the moments equation on the proximal phalange around the proximal joint:

16) $$\sum M_{pj} = F_{r,y} \cdot L_1 \cdot \cos(\theta_p) - F_{r,x} \cdot L_1 \cdot \sin(\theta_p) - F_1 \cdot L_0 = 0$$

Single contact

In case only the proximal phalange is in contact the same equilibrium equations should hold, except now F_2 is zero and θ_d is not known on forehand. Equation 11 can be rewritten, after setting $F_2 = 0$ and division by c, to the following function of θ_d only:

17) $f(\theta_d) = F_a \cdot \sin(\angle 3) - F_s \cdot \sin(\angle 3_c)$

For the distal phalange to be in equilibrium $f(\theta_d)$ should be zero, i.e. the moment generated by the actuation force should exactly balance the moment due to the spring force. This nested equation can be solved numerically for θ_d, thereby defining the static equilibrium position for a given actuation torque and spring stiffness. Now the attitude of the finger is known equations 10 – 15 can be reused to compute the contact forces, where F_2 should obviously end up being zero.

Figure 28, a plot of $f(\theta_d)$ for various parameter values, shows that for increasing actuation torques the function shifts upwards, until at a certain point the graph does no longer have a zero crossing in the accessible range of angles. A positive resulting moment causes an increase whereas a negative moment leads to a decrease in θ_d, hence the marked equilibriums are all asymptotically stable and all equilibrium positions on the right of the local minimum are unstable. In this region the angle increases until the maximum accessible angle is reached and the joint hits its mechanical constraint.

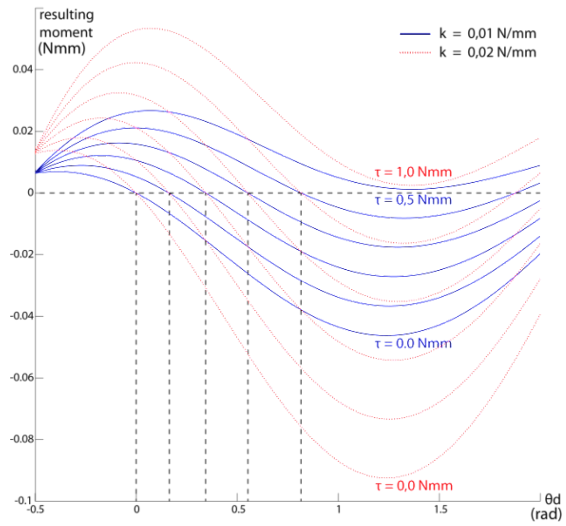

Figure 28: $f(\theta_d)$ *plotted for a range of torques and 2 values for the spring stiffness. Parameters used:* L_0=15, L_1=30, L_2=20.8, a=10.7, b=27, c=5, $\angle 5$=2.3

Merged model

To successfully merge both models a validation condition is defined on the distal phalange's contact force, i.e. when according to the full contact model $F_2 < 0$ the phalange is not in contact and the single contact model is valid, for $F_2 \geq 0$ the distal phalange is in contact and the full contact model is valid. Furthermore a constraint on the first contact force is added ($F_1 \geq 0$) since, similarly to prior case, a negative contact force corresponds to a transition of configuration, in this case to a grasp where only the distal phalanges and the palm are in contact with the object, provided that $\theta_p - \theta_d \leq 0$ to ensure the object is still enveloped properly.